

We are IntechOpen, the world's leading publisher of Open Access books Built by scientists, for scientists

6,900

Open access books available

186,000

International authors and editors

200M

Downloads

Our authors are among the

154

Countries delivered to

TOP 1%

most cited scientists

12.2%

Contributors from top 500 universities



WEB OF SCIENCE™

Selection of our books indexed in the Book Citation Index
in Web of Science™ Core Collection (BKCI)

Interested in publishing with us?
Contact book.department@intechopen.com

Numbers displayed above are based on latest data collected.
For more information visit www.intechopen.com



Doppler Radar for USA Weather Surveillance

Dusan S. Zrnic
NOAA, National Severe Storms Laboratory
USA

1. Introduction

Weather radar had its beginnings at the end of World War II when it was noticed that storms clutter radar displays meant to reveal enemy aircraft. Thus radar meteorology was born. Until the sixties only the return power from weather tracers was measured which offered the first glimpses into precipitation structure hidden inside clouds. Possibilities opened up to recognize hail storms, regions of tornadoes (i.e., hook echoes), the melting zone in stratiform precipitation, and even determine precipitation rates at the ground, albeit with considerable uncertainty.

Technology innovations and discoveries made in government laboratories and universities were quickly adopted by the National Weather Service (NWS). Thus in 1957 the Miami Hurricane Forecast Center commissioned the first modern weather radar (WSR-57) the type subsequently installed across the continental United States. The radar operated in the 10 cm band of wavelengths and had beamwidth of about 2°. In 1974 more radars were added: the WSR-74S operating in the band of 10 cm wavelengths and WSR-74C in the 5 cm band.

Development of Doppler radars followed, providing impressive experience to remotely observe internal motions in convective storms and infer precipitation amounts. Thus scientists quickly discovered tell tale signatures of kinematic phenomena (rotation, storm outflows, divergence) in the fields of radial velocities.

After demonstrable successes with this technology the NWS commissioned a network of Doppler radars (WSR-88D=Weather Surveillance Radars, year 1988, Doppler), the last of which was installed in 1997. Much had happened since that time and the current status pertinent to Doppler measurements and future trends are discussed herein.

The nineties saw an accelerated development of information technology so much so that, upon installation of the last radar, computing and signal processing capabilities available to the public were about an order of magnitude superior to the ones on the radar. And scientific advancements were still coming in strong implying great improvements for operations if an upgrade in processing power were to be made. This is precisely what the NWS did by continuing infusion of the new technology into the system. Two significant upgrades have been made. The first involved replacement of the computer with distributed workstations (on the Ethernet in about 2002) for executing algorithms for precipitation estimation, tornado detection, storm tracking, and other. The second upgrade (in 2005)

brought in fully programmable signal processor and replaced the analogue receiver with the digital receiver. In 2009 the NWS started the process of converting the radars to dual polarization which should be accomplished by mid 2013.

The number of radars used continuously for operations is 159 and there are two additional radars for other use. One is for supporting changes in the network brought by infusion of new science or caused by deficiencies in existing components (designated KCRI in Norman, OK). The evolution involves both hardware and software and the update in the former are typically made annually. The other (designated KOUN in Norman, OK, USA) is for research and development. Therefore its configuration is more flexible allowing experimental changes in both hardware and software.

Conference articles and presentation about the WSR-88D and its data abound and there are few descriptions of its basic hardware. Very recent improvements are summarized by Saxion & Ice (2011) and a look into the future is presented in Ice & Saxion (2011). Yet only few journal articles describing the system have been published. The one by Heiss et al. (1990) presents hardware details from the manufacturer's point of view. The paper by Crum et al. (1993) describes data and archiving and the one by Crum & Albery (1993) contain valuable information about algorithms. The whole No. 2 issue of *Weather and Forecasting* (1998), Vol. 13 is devoted to applications of the WSR-88D with a good part discussing products that use Doppler information. A look at the network with the view into the future is summarized by Serafin & Wilson (2000).

As twenty years since deployment of the last WSR-88D is approaching there are concerns about future upgrades and replacements. High on the list is the Multifunction Phased Array Radar (MPAR). At its core is a phased array antenna wherein beam position and shape are electronically controlled allowing rapid and adaptable scans. Thus, observations of weather (Zrnic et al., 2007) and tracking/detecting aircraft for traffic management and security purposes is proposed (Weber et al., 2007). Another futuristic concept is exemplified in proposed networks for Cooperative Adaptive Sensing of the Atmosphere (CASA) consisting of low power 3 cm wavelength phased array radars (McLaughlin et al., 2009).

Very few books on weather radar have been written and most include Doppler measurements. Here I list some published within the last 20 years. The one by Doviak & Zrnic (2006) primarily concentrates on Doppler aspects and contains information about the WSR-88D. The book by Bringi & Chandrasekar (2001) emphasizes polarization diversity and has sections relevant to Doppler. Role of Doppler radar in aviation weather surveillance is emphasized in the book by Mahapatra (1999). The compendium of chapters written by specialists and edited by Meishner (2004) concentrates on precipitation measurements but has chapters on Doppler principles as well as application to severe weather detection. *Radar for meteorologists* (Rinehart, 2010) is equally suited for engineers, technicians, and students who will enjoy its easy writing style and informative content.

2. Basic radar

The surveillance range, time, and volumetric coverage are routed in practical considerations of basic radar capabilities and the size and lifetimes of meteorological phenomena the radar is supposed to observe. This is considered next.

2.1 Considerations and requirements for storm surveillance

Table 1 lists the radar parameters with which the surveillance mission is supported. Discussions of the reasons behind choices in volume coverage and other radar attributes of the WSR-88D network, with principal emphasis on Doppler measurements, follows.

Requirement	Values
Surveillance: Range Time Volumetric coverage	460 km < 5 min hemispherical
SNR	> 0 dB, for Z= - 8 dBZ at r=50 km (exceeded by ~5 dB)
Angular resolution	≤1°
Range sampling interval: For reflectivity For velocity	$\Delta r \leq 1$ km; $0 < r \leq 230$ km; $\Delta r \leq 2$ km; $r \leq 460$ km $\Delta r = 250$ m
Estimate accuracy: Reflectivity Velocity Spectrum width	≤1 dB; SNR>10 dB; $\sigma_v = 4$ m s ⁻¹ ≤1 m s ⁻¹ ; SNR> 8 dB; $\sigma_v = 4$ m s ⁻¹ ≤1 m s ⁻¹ ; SNR>10 dB; $\sigma_v = 4$ m s ⁻¹

Table 1. Requirements for weather radar observations.

2.1.1 Range

Surveillance range is limited to about 460 km because storms beyond this range are usually below the horizon. Without beam blockage, the horizon’s altitude at 460 km is 12.5 km; thus only the tops of strong convective storms are intercepted. Quantitative measurements of precipitation are required for storms at ranges less than 230 km. Nevertheless, in the region beyond 230 km, storm cells can be identified and their tracks established. Even at the range of about 230 km, the lowest altitude that the radar can observe under normal propagation conditions is about 3 km. Extrapolation of rainfall measurements from this height to the ground is subject to large errors, especially if the beam is above the melting layer and is detecting scatter from snow or melting ice particles.

2.1.2 Time

Surveillance time is determined by the time of growth of hazardous phenomena as well as the need for timely warnings. Five minutes for a repeat time is sufficient for detecting and confirming features with lifetime of about 15 min or more. Typical mesocyclone life time is 90 minutes (Burgess et al., 1982). Ordinary storms last tens of minutes but microbursts from these storms can produce dangerous shear in but a few minutes. Similarly tornadoes can rapidly develop from mesocyclones. For such fast evolving hazards a revisit time of less than a minute is desirable but not achievable if the whole three dimensional volume has to be covered. The principal driver to decrease the surveillance time is prompt detection of the tornadoes so that timely warning of their presence can be issued. Presently, the lead time for tornado warnings (i.e., the time that a warning is issued to the time the tornado does damage) is about 12 minutes (see Section 5).

2.1.3 Volumetric coverage

The volume scan patterns currently available on the WSR-88D have maximum elevations up to 20° and many are accomplished in about 5 minutes. Meteorologists have expressed a desire to extend the coverage to higher elevations to reduce the cone of silence. It is fair to state that the 30° elevation might be a practical upper limit for the WSR-88D. Top elevations higher than 20° have not been justified by strong meteorological reasons.

2.1.4 Signal to noise ratio

The SNR listed in Table 1 provides the specified accuracy of velocity and spectrum width measurements to the range of 230 km for both rain and snowfall rates of about 0.3 mm of liquid water depth per hour. That is, at a range of 230 km the SNR is larger than 10 dB thus the accuracy of Doppler measurements to shorter ranges is independent of noise and solely a function of number of samples and Doppler spectrum width.

2.1.5 Spatial resolution

The angular resolution is principally determined by the need to resolve meteorological phenomena such as tornados and mesocyclones to ranges of about 230 km, and the practical limitations imposed by antenna size at wavelength of 0.1 m. Even though beamwidth of 1° provides relatively high resolution, the spatial resolution at 230 km is 4 km. Because the beam of the WSR-88D is scanning azimuthally, the effective angular resolution in the azimuthal direction is somewhat larger (Doviak & Zrnic, 2006, Section 7.8); typically, about 40% at the 3 RPM scan rates of the WSR-88D. This exceeds many mesocyclone diameters, and thus these important weather phenomena, precursors of many tornadoes, can be missed. Tornadoes have even smaller diameters and therefore can not be resolved at the 230 km range.

The range resolution is indirectly influenced by the angular resolution; there is marginal gain in having range resolution finer than the angular one. For example better range resolution can provide additional shear segments and therefore improve detection of vortices at larger distance. The range resolution for reflectivity is coarser for two reasons: (1) reflectivity is principally used to measure rainfall rates over watersheds which are much larger than mesocyclones and (2) reflectivity samples at a resolution of 250 m are averaged in range (Doviak & Zrnic, 2006, Section 6.3.2) to achieve the required accuracy of 1 dB.

2.1.6 Precision of measurements

The specified 1 dB precision of reflectivity measurements (Table 1) provides about a 15% relative error of stratiform rain rate (Doviak & Zrnic, 2006, eq 8.22a). This has been accepted by the meteorological community. The specified precisions of velocity and spectrum width estimates are those derived from observations of mesocyclones with research radars. The 8 dB SNR is roughly that level beyond which the precision of velocity and spectrum width estimates do not improve significantly (Doviak & Zrnic, 2006, Sections 6.4, 6.5). But, it is possible that lower precisions can be tolerated and benefits can be derived therefrom. For example, it has been proposed (Wood et al., 2001) that velocity estimates be made with less samples (e.g., by a factor of two) in order to improve the azimuthal resolution. Although

this increases the error of the Doppler velocity estimates by the square root of two, the improved angular resolution can increase the range, by about 50% (Brown et al., 2002 and 2005), to which mesocyclones and violent tornadoes can be detected. Therefore in the recently introduced scanning patterns, the data (i.e., spectral moments) are provided at 0.5° increments in azimuth (Section 3.5).

2.2 Radar operation

The essence of the hardware (Fig. 1) is what radar operators see on the console. To the left of the data link (R,V,W,D) is the radar data acquisition (RDA) part consisting of the transmitter, antenna, microwave circuits, receiver, and signal processor. These components are located at radar site and data is transmitted to the local forecast office (LFO) where Radar Product Generation (RPG, Fig. 1) takes place. Operators at the LFO control (the block Control in Fig. 1) the radar and observe/analyze displays of data fields. At a glance of a console they can see the operating status of the radar and data flow. In the RPG the data is transformed into meteorologically meaningful information (Products in Fig. 1) by algorithms executed on Ethernet cluster of workstation.

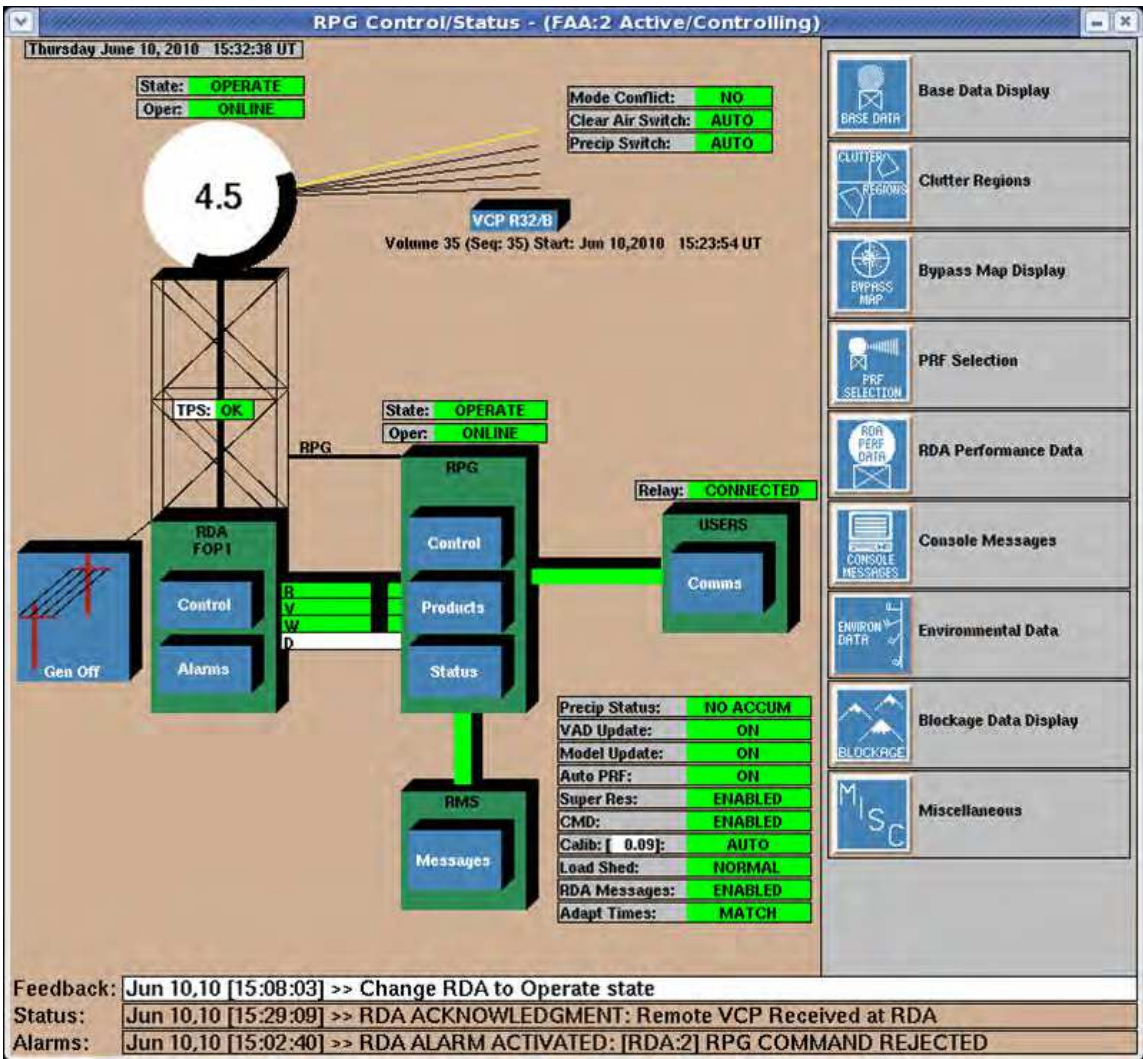


Fig. 1. Block diagram of the WSR-88D seen on the console of operators.

The radar is fully coherent pulsed Doppler and pertinent parameters are listed in Table 2 (see also Doviak & Zrnic, 2006 page 47). Each radar is assigned a fixed frequency in the band (Table 2), hence some values like the beamwidth and unambiguous velocities (not listed) depend on the exact frequency.

Frequency Beamwidth Antenna gain	2.7 to 3 GHz 1° 44.5 to 45.5 dB
Transmitter: Pulse power Pulse width Rf duty cycle PRFs (Hz, 5 sets of 8, variation ~3%) Unambiguous range (km)	750 kW 1.57 μs and 4.57 μs 0.002 322, 446, 644, 857, 1014, 1095, 1181, 1282 466, 336, 233, 175, 148, 137, 127, 117
Receiver linear: Dynamic range Intermediate frequency (IF) A/D converter at IF Sampling rate Noise figure	94 dB at 1.57 μs pulse and 99 dB at 4.57 μs 57.6 MHz 14 bits 71.9 MHz -113 dBm at 1.57 μs and -118 dBm at 4.57 μs
Filter bandwidth or type: Front end analogue IF Digital matched, short/long pulse Radial spacing in azimuth	6 MHz (3 dB bandwidth) Output samples spaced at 250 m/500m 1° or 0.5°

Table 2. Radar characteristics.

The data coming out of the RDA consist of housekeeping (time, pointing direction of the antenna, status, operating mode, and fields of reflectivity factor, mean radial velocity, and spread of velocities (designated as R, V, W in the console, Fig. 1), collectively called spectral moments. A wideband communication link is used to exchange base data and radar status/control between RDA and RPG. Depending on distance this link is by direct wire (up to 120 m), microwave line-of-site (to 38 km), or telephone company T1 line (unlimited).

Pulse of high peak power and narrow width (Table 2) generated at the output of the power amplifier is guided to the antenna. It is radiated in form of electromagnetic (EM) field confined within the narrow (1°) antenna beam. The propagating EM field interacts with intervening scatterers (precipitation, biological, and other). Part of the field is reflected forming a continuous stream at the antenna where it is intercepted and transformed for further processing by the receiver. Concise mathematical expression for the magnitude of the electric field at a distance r from the radar is

$$E = \left[\frac{P_a \eta}{\pi} \right]^{1/2} \frac{f(\theta, \phi)}{2r} \cos \left[2\pi f \left(t - \frac{r}{c} \right) + \psi_t \right] U(t - r / c), \tag{1}$$

where P_a is the power radiated by the antenna, r is the distance, $f(\theta, \phi)$ is the antenna pattern function (one way voltage), η is the free space impedance ($120\pi \Omega$), c speed of light, f radar frequency, and ψ_t arbitrary phase at the antenna. $U(t-r/c)$ designates the pulse function such that it is 1 if its argument is between 0 and τ (the pulse width).

2.2.1 Radar signal and Doppler shift

The effective beam cross section and pulse width define the intrinsic radar resolution volume but processing by the receiver increases it in range. Scatterers (hydrometeors such as rain, hail, snow and also insects, birds etc.,) within the resolution volume contribute to the backscattered electric field which upon reception by the antenna is transformed into a microwave signal. The signal is converted to an intermediate frequency f_{if} then passed through anti-alias filter (nominal passband ~ 14 MHz), digitized (as per Table 2), and down converted to audio frequencies (base band) for further processing.

At intermediate frequency the signal coming from a continuum of scatterers can be represented as $A(t)\cos(\omega_{if}t + \omega_d t)$ where the amplitude $A(t)$ fluctuates due to contribution by scatterers and ω_d is the instantaneous Doppler shift caused by their motions toward (positive shift) and/or away (negative shift) from the radar. To determine the mean sense of motion (sign of Doppler shift) the intermediate frequency is removed and the signal is decomposed into its sinusoidal and cosinusoidal components, the inphase I and quadrature phase Q parts. These carry information about the number and sizes of scatterers as well as their motion. Samples of I and Q components are taken at consecutive delays with respect to the transmitted pulse. The delays are proportional to the range within the cloud from which the transmitted pulse is reflected. Samples from the same range locations (delays) are combined to obtain estimates of the spectral moments: reflectivity factor Z , mean Doppler velocity v , and spectrum width σ_v (Doviak & Zrnic, 2006). The Doppler velocity v is related to the frequency shift f_d and wavelength λ via the Doppler equation

$$f_d = 2v/\lambda, \quad (2)$$

and so is the spectrum width.

Radars display (and store) equivalent reflectivity factor (often denoted with Z_e) which is computed from the power and other parameters in the radar equation (Doviak & Zrnic 2006) assuming the scatterers have refractive index of liquid water. For small (compared to wavelength) spherical scatterers, Z_e expressed as function of the distribution of sizes $N(D)$, equals

$$Z_e = \int_0^{D_{\max}} N(D) D^6 dD. \quad (3)$$

2.2.2 Processing path from signals to algorithms

Top left part in Fig 2 illustrates the continuum of returns (either I or Q), after each transmitted pulse from 1,...to M . Thus M samples at a fixed range delay (double vertical line) are operated on in various ways to produce estimates. There are as many estimates

along range time as there are samples. That is, sample spacing is typically equal to pulse duration and therefore consecutive samples are almost independent. Closer sampling (i.e., oversampling) has some advantages (Section 4.2).

Radials of spectral moments are transmitted to the RPG (a radial of velocities is in the top right part of Fig. 2). Spectral moments are displayed at Weather Forecast Offices, are recorded, and are also processed by algorithms to automatically identify hazardous weather features, estimate amounts of precipitation, and to be used in numerical models among other applications. Example displayed in Fig. 2 (right bottom) is the field of Doppler velocities obtained by the WSR-88D in Dove, North Carolina during the Hurricane Irene on Aug 28th, 2011 at 2:29 UTC. The end range on the display is 230 km which is also the range up to which quantitative measurements are currently being made. Extension to 300 km is planned.

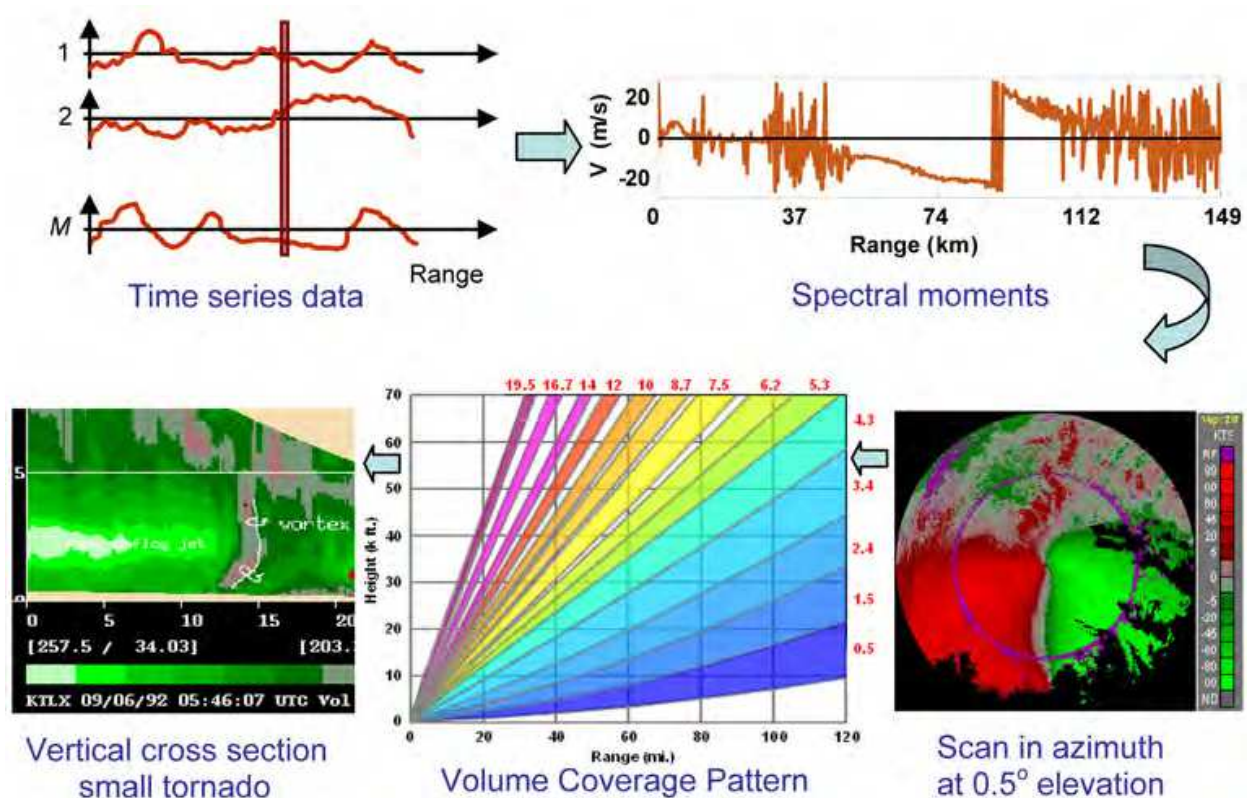


Fig. 2. Information path from time series to output of algorithms.

The radar is sufficiently sensitive to detect precipitation at much larger ranges where the beamwidth and observations high above ground mar quantitative interpretation of impending weather on the ground. At the elevation of 0.5°, the radar makes two scans: one with the longest PRT (3.1 ms) for estimating reflectivities unambiguously up to 465 km in range, the other with one of the short PRTs to estimate unambiguously velocity over a sufficiently large span. The ambiguities in range and velocity are inherent to pulsed Doppler radars. Reflections from scatterers spaced by the unambiguous range ($r_a = cT_s/2$ where T_s is pulse repetition time) appear at the same delay with respect to the reference time (determined by the last of two transmitted pulse). Obvious increase in range can be made by increasing T_s . And this is fine for measurements of reflectivity but would harm measurements of velocity. At the 10 cm wavelength Doppler velocities are

estimated from the change in phase of the returned signal (Doviak & Zrnic 2006). Thus the WSR-88D is a phase sampling and measuring instrument. The change in phase of the return from one pulse to the next $2\pi f_d T_s$ is proportional to the Doppler velocity v as indicated in (2).

If the phase change caused by precipitation is outside the $-\pi$ to π interval it cannot be easily distinguished from the change within this interval. These limits define the unambiguous frequency $f_a = \pm 1/(2T_s)$ and through the Doppler relation (2) the unambiguous velocity as

$$v_a = \lambda/(4T_s). \quad (4)$$

Scatterers do cause a Doppler shift within the pulse as it is propagating and reflecting, but this shift is very small and can not be measured reliably as the following argument demonstrates. Consider the $\tau = 1.57 \mu\text{s}$ pulse width (WSR-88D) and scatterers moving at 10 m s^{-1} (36 km h^{-1}). The corresponding Doppler frequency shift is 200 Hz (at 10 cm wavelength) and it produces a phase difference of 0.11° ($2\pi f_d \tau$) between the beginning and end of the pulse return. This tiny difference can not be measured with sufficient accuracy to yield useful estimate.

To mitigate the ambiguity problem the WSR-88D has some options one of which is special phase coding and processing. The result is seen in Fig. 2 where the pink ring at 137 km indicates the unambiguous range for velocity measurements (see discussion in section 3.2.3); it represents censored data because the ground clutter from nearby range and weather signals from the second trip range are comparable in power and can not be reliably separated.

Operators of the WSR-88D have at their disposal preprogrammed volume coverage patterns (VCP – see example in Fig. 2). These are consecutive scans starting from elevation of 0.5° and incrementing until a top elevation is reached. Most algorithms require a full volume scan to generate a product. The one in Fig. 2 (bottom left) reconstructs a vertical profile of Doppler velocities along a radial; the radar is located to the right and green colors indicate velocities toward the radar in 5 m s^{-1} increments starting with 0 (gray color). Cylindrical protrusion below 5 km in the middle with some velocities toward the radar (red color) is indicative of a tornado.

3. Signal processing and display

The block diagram (Fig. 3) of the WSR-88D radar is typical for pulsed Doppler radars. Essential components are the Frequency and Timing generator, the transmitter and the receiver. Radar and antenna controls are omitted from the figure. Intermediate frequency (if) on the radars is 57.6 MHz , and the local oscillator (lo) frequency is adjustable to cover the range between 2.7 and 3 GHz (the operating band, see Table 2). The power amplifier is a klystron. The transmit/receive switch is comprised of a circulator and additional devices to protect the receiver from the transmitted high power pulse. The low noise amplifier (LNA) has a noise figure $\sim 0.8 \text{ dB}$ and the receiver bandwidth is 6 MHz up to the input of the digital receiver. The digital receiver is a proprietary product of SIGMET Co (now Vaisala) and its essence is described next.

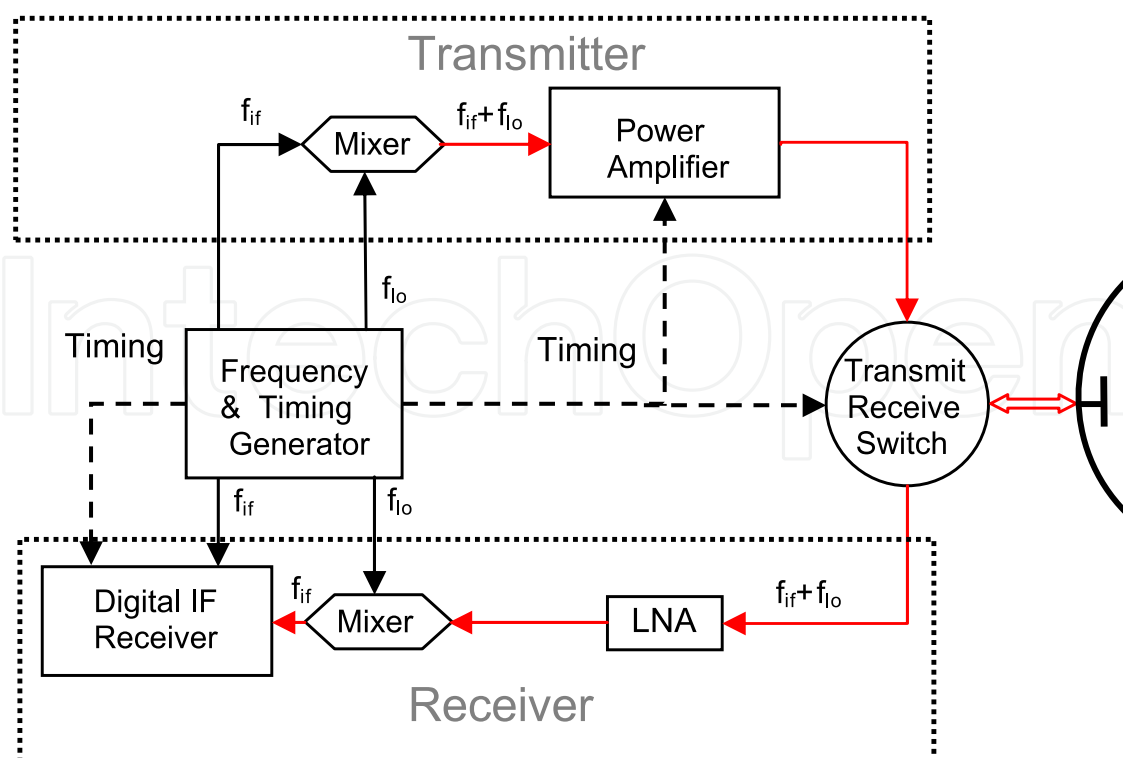


Fig. 3. Block diagram of the receiver (without signal processing part) and the transmitter.

3.1 Digital receiver

The analogue signal $A(t)\cos(\omega_{if}t + \omega_d t)$ is sampled at a rate of 71.9 MHz producing a stream (time t_i) of 14 bit numbers. These are multiplied (Fig. 4) with $\sin(\omega_{if}t_i)$ and $\cos(\omega_{if}t_i)$ and digitally filtered to obtain the base band I and Q components (at times t_k). Although the nominal short pulse duration is $1.57 \mu\text{s}$ same as sample spacing in range, 155 samples spaced at $\sim 13.8 \text{ ns}$ over $2.15 \mu\text{s}$ interval are used for multiplication and filtering (in the long pulse mode the number of samples is 470 over a $6.53 \mu\text{s}$ interval). The digital low pass filter is adjusted to match the shape of the transmitted long or short pulse. Matching is achieved by passing the attenuated transmitted pulse ("burst") through the receiver and taking the discrete Fourier transform of the output. The inverse of this transform gives the coefficients of the matched impulse response filter. Amplitude and phase of the "burst" is sampled upon each transmission to monitor power, compensate for phase instabilities, and use in phase codes for mitigating range ambiguities. The timing diagram (Fig. 5) illustrates the relations between transmitted sequence, digital oscillator samples, the sampled sequence from a point scatterer and its I and Q values (after the matched filter).

3.2 Transmitted sequences and volume scans

Several volume coverage patterns are available. With the exception of one all utilize the short pulse. The exception has a uniform sequence of long pulses at the longest PRT for observations in clear air or snow where weak reflections are from insects, birds, ice and/or refractive index fluctuations. For storm observations the volume coverage patterns have three distinct modes depending on the elevation.

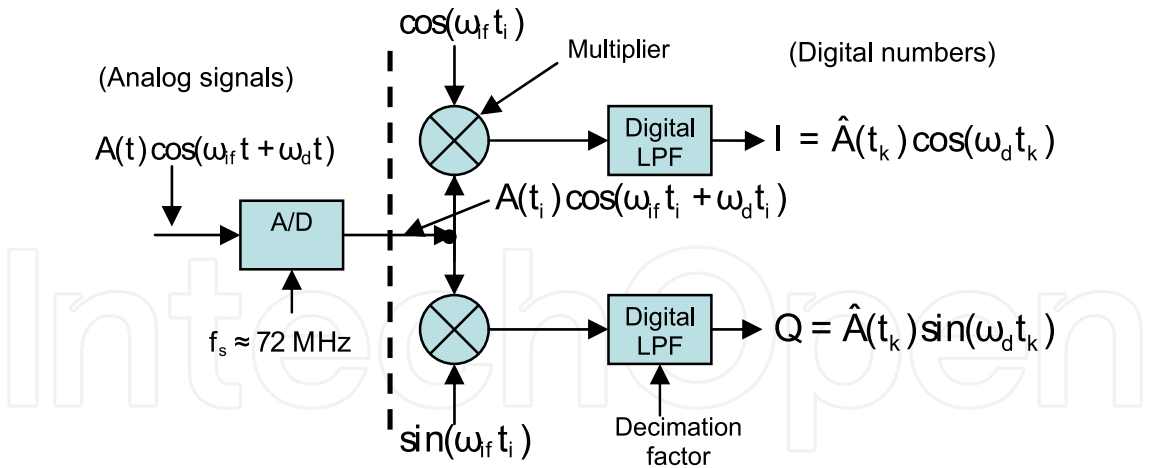


Fig. 4. Conceptual diagram of the digital receiver and down converter indicating the essential operations. The dashed vertical line shows where digital processing begins.

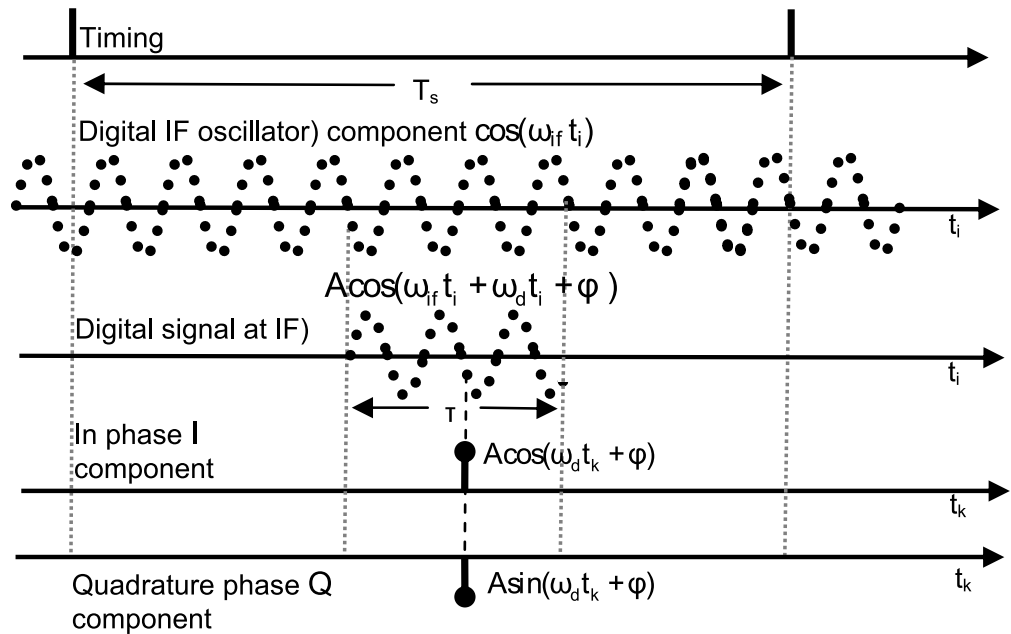


Fig. 5. Conceptual timing diagram of processes in the digital receiver. The return signal is assumed to be sinusoidal pulse such as would be produced by a single point scatterer.

3.2.1 Lowest elevation scans

At the lowest two (sometime three) elevations ($< 1.6^\circ$) two consecutive scans at each elevation are made. For surveillance and reflectivity measurement the longest PRT is used so that the unambiguous range is $\sim 460 \text{ km}$. It is followed by one or more of the higher PRTs for measurement of Doppler velocity and spectrum width whereby the unambiguous velocity interval is larger than $\sim 20 \text{ m s}^{-1}$. Thus Doppler estimates can be ambiguous and overlaid in range. To determine the location of the Doppler estimates, powers along the radial at the same azimuth but in the surveillance scans are examined. The echoes from ranges spaced by $n\text{PRT}c/2$ of the Doppler scan, where n is 1, 2, 3, 4, can be overlaid in the Doppler scan; the echo for $n=1$ is said to come from the first trip because it corresponds to the round trip shorter than the separation between consecutive pulses. Powers from

locations spaced by $nPRT_c/2$ are compared to determine the correct range of the Doppler estimates and presence of overlaid echoes. If one of the overlaid powers is larger than user specified threshold (typically 5 dB) the corresponding Doppler spectral moment is assigned to the correct range whereas the values at location of the other overlaid echoes are censored. If the powers are within 5 dB, the variables at all locations where the overlay is possible are censored. Because the Doppler spectral moments are computed and recorded only to the distance of at most twice the unambiguous range the censoring is also done to that distance.

There is a special VCP (Zittel et al., 2008) with three scans at same elevation on five consecutive lowest elevations whereby velocities from three PRFs (No. 4, 6, and 8 in table 2) are combined to increase the v_a and display it up to the distance of 175 km.

3.2.2 Scans at mid and high elevations

At elevations between 1.6° and 7° a “batch” sequence is transmitted. It is a dual PRF in which the first few (3 to 12) pulses are at the lowest PRF and the rest (between about 25 and 90) are transmitted at one of the four highest PRFs (shortest PRTs, Table 2). The lowest PRF pulses are for surveillance, reflectivity measurements, and censoring and assignment of range to Doppler spectral moments; just the same as in the lowest scans. To improve accuracy of the reflectivity estimates powers from the Doppler sequence (high PRF) are included in the averaging provided there is no contamination by overlaid echoes. Beyond 7° elevation uniform PRTs are transmitted because the tops of storms at locations where overlay can occur are below the radar beam.

3.2.3 Phase coding

To mitigate range overlay some volume scanning patterns at the lowest elevations ($<2^\circ$) have transmitted sequences encoded with the SZ(8/64) phase code (Sachidananda & Zrnic, 1999). The concept is depicted in Fig. 6 and explained in the caption. The prescribed phases Ψ_k (i.e., switching phases) are applied to the transmitted pulses. Formally this is represented by multiplication of the sequence with the switching code $a_k = \exp(j\Psi_k)$. The first trip return signal is made coherent by multiplying it with the conjugate $a_k^* = \exp(-j\Psi_k)$. With this multiplication the 2nd trip signal is phase modulated by the code $c_k = a_{k-1}^* a_k$. The 2nd trip can be made coherent by multiplying the incoming sequence with a_{k-1} , in which case the 1st trip signal is modulated by the code c_k^* . The code, a_k is designed such that the modulation code c_k has a phase shift given by $\varphi_k = \Psi_{k-1} - \Psi_k = 8\pi k^2 / 64$. The special property of this code is that its autocorrelation is unity for lags in multiples of 8 (lags $8n$; $n=0,1,2,\dots$), and is zero for all other lags. Therefore the power spectrum has only 8 non-zero coefficients separated by $M/8$ coefficients. The SZ(8/64) switching code is given by

$$a_k = \exp[-j \sum_{m=0}^k (\pi m^2 / 8)]; \quad k=0,1,2,\dots,63. \quad (5)$$

It has periodicity of 32 hence the number of samples M must be an integer multiple of 32. From (5) it is obvious that the phase sequence consists of a binary sub multiple of 360° hence it is generated without round-off errors using standard binary phase shifters. Because the

desired phase and actual phase might not be exactly equal, the transmitted phase is sampled and used in processing to precisely cohere the signal from the desired trip.

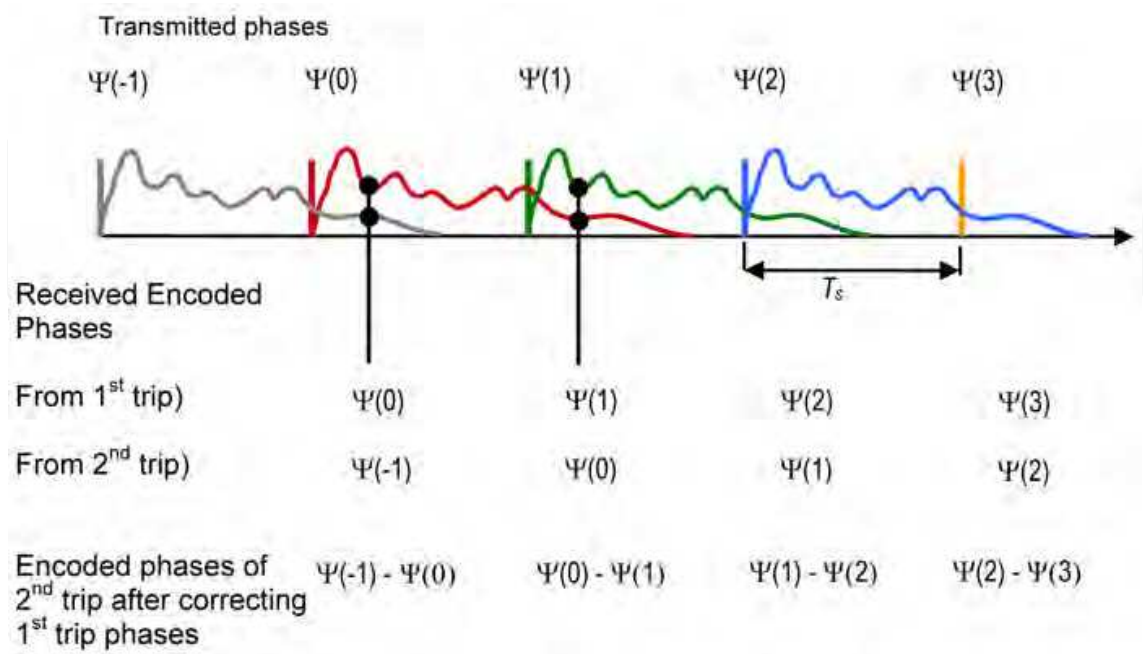


Fig. 6. Transmitted pulse sequence (vertical color lines) and the corresponding received powers (wiggly curves). The phases of the transmitted pulses are indicated and indexed from -1 to 3. The location of overlay at one fixed range is indicated by two black vertical lines. The phases of the received signals from the first and second trip are indicated as well as the phase of the second trip signal after subtracting (correcting) the phase of the first trip.

In case of overlaid echoes the phase coding allows separation of the contributions by the first and second trip signals. This is accomplished by first cohering (correcting) the phases of the stronger echo, then filtering it out. For example if first trip is cohered the second trip signal spectrum (complex with magnitudes and phases) is split into eight replicas over the unambiguous interval. Then frequency domain filtering of the first (strong) trip signal with a notch centered on its spectrum and having a width of $\frac{3}{4}$ unambiguous interval leaves two spectral replicas of the second trip signal spectrum. From these replicas it is possible to reconstruct the second trip spectrum and compute spectral moments. It turns out that cohering for the first trip signal induces 4 spectral replicas in the third trip signal and again eight replicas into the fourth trip signal; the fifth trip signal has two replicas and can not be recovered.

Determination of the ranges where overlaid echoes might be is made using powers from the surveillance scan (long PRT) which precedes the Doppler scan (phase coded short PRT). The overlay trip number and powers are needed to make proper cohering-recohering order and notch filter application. In case ground clutter is present Blackman window is applied to time series data and clutter is taken out with a special frequency domain filter (Sec 3.3). If there is no clutter contamination but overlaid echoes are present the von Hann window is chosen. An example of Doppler velocity fields obtained with the SZ(8/64) phase code is in Fig. 7 (left side). The same field obtained by processing and censoring with no phase coding is also plotted (right side); note the large pink area in the second trip region indicative of non recoverable velocities. Small pink areas in the first trip region (SE of radar) signify that

overlaid powers of first and second trip signals are within 10 dB and hence velocities can not be confidently recovered. There is a narrow pink ring of censored data in the image where phase code is applied. The beginning range of the ring is at the start of the second trip (175 km) and is caused by automatic receiver shut down during transmission followed by the strong first trip ground clutter overwhelming the weaker second trip signal.

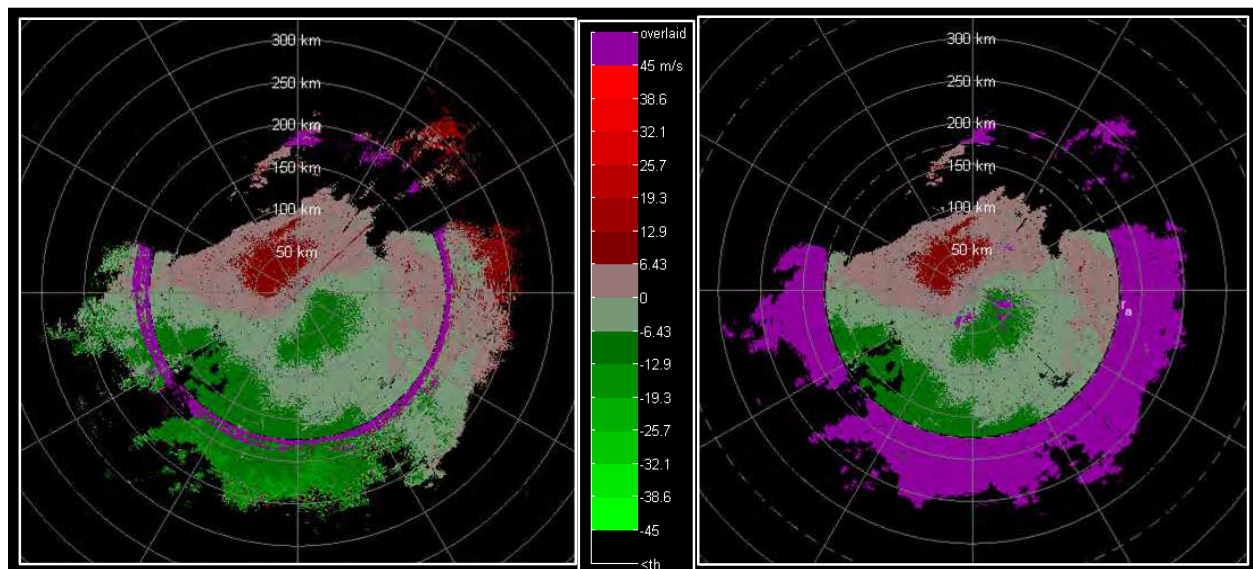


Fig. 7. Fields of Doppler velocities. Left: obtained from phased coded sequence. Right: obtained from non coded sequences. Elevation is 0.5° , the unambiguous velocity $v_a = 23.7 \text{ m s}^{-1}$ and range $r_a = 175 \text{ km}$. Data were collected on 10/08/2002 with the research WSR-88D (KOUN). The color bar indicates velocities in m s^{-1} . (Figure from Torres et al., 2004c).

3.3 Ground clutter filter

The ground clutter filter implemented on the network is a frequency domain filter with interpolation over the removed clutter spectral coefficients. The filter called Gaussian Model Adaptive Processing (GMAP) has been developed by Siggia and Passarelli (2004). Its first premise is: clutter has a Gaussian shape power spectrum with width linearly related to the antenna rotation rate; hence the width can be computed. The second is the signal spectrum has also Gaussian shape and has width larger than clutter's. The Blackman window is applied followed by Fourier transform. Receiver noise is externally provided to the filter and used to establish the spectral noise level which helps determine how many spectral coefficients either side of zero to remove (Fig. 8, blue peak is from ground clutter). The removed coefficients are replaced (iteratively) with a Gaussian curve obtained from Doppler moments and the spectrum of the weather signal (dotted curve) is restored. Then the inverse discrete Fourier transform is performed to obtain the autocorrelation at lag 1. The argument of the autocorrelation is linearly related to the mean Doppler velocity (see section 3.4).

Several options exist to decide where to filter clutter. One relies on the clutter map to locate azimuths and ranges. It is also possible but undesirable to apply clutter filter everywhere. The operators can select regions between azimuths and ranges where to turn the filter on. Recently an adaptive algorithm called Clutter Mitigation Decision has been implemented (Hubbert et al., 2009). It uses coherency of the clutter signal exemplified in what the authors

call Clutter Phase Alignment (CPA) defined as $CPA = |\sum V_k| / \sum |V_k|$, where V_k is the complex voltage ($I + j Q$) from a fixed clutter location at consecutive times (spaced by the PRT) indicated by time index k and the sum is over the total number of pulses in the dwell time. Local standard deviation (termed texture) of reflectivity factor Z_i in range (i index indicates adjacent values in range) and changes in sign of the differences $Z_{i+1} - Z_i$ are also used; the frequency of change in reflectivity gradient along range is obtained from this difference and it defines the spin variable. The CPA, texture, and spin are combined in a fuzzy classification scheme to identify locations where clutter filter should be applied.

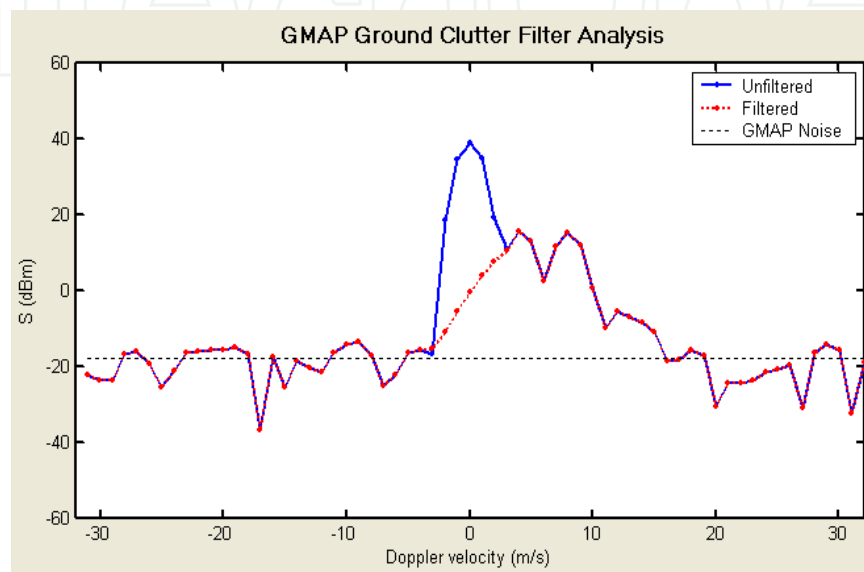


Fig. 8. Doppler spectrum of simulated weather signal (red) and clutter (blue). Interpolated (filtered) Gaussian part and estimated noise level are shown. The $v_a = 32 \text{ m s}^{-1}$. (Figure as in Torres et al., 2004c).

The GMAP filter and censoring (Free & Patel, 2007) is applied to surveillance and Doppler scans. In the “batch” mode the number of samples is insufficient for spectral processing hence the average voltage (i.e., DC) from the samples spaced by the long PRT is removed.

The system also employs strong point clutter (typically caused by aircraft) removal along radials. It is done on each spectral moment independently by comparing the sample power with two adjacent values either side of it. If the value is outside prescribed criteria it is replaced by interpolation of neighboring values.

3.4 Computation of spectral moments

In computations of Z and σ_v receiver noise powers are subtracted from the returned powers. Thus, the receiver noise power is estimated at the end of each volume scan at high elevation angle. The noise depends on the elevation angle because contributions from ground radiation and air constituents are larger if the beam is closer to the ground. To account for the increase the noise is extrapolated to lower elevations using empirical relations.

The reflectivity factor is obtained by summing the pulse powers, subtracting the noise power, and using the radar equation (Doviak & Zrnic, 2006). At the lowest few elevations Z is computed from the long PRT (surveillance scan). At mid elevations (“batch mode”) the

reflectivity is computed from both the long and short PRTs if no overlay is indicated; otherwise only samples from the surveillance scan (long PRT) are used.

Computation of Doppler variables starts with the discrete Fourier transform. In absence of clutter, time series data is equally weighted (uniform window) and the power spectrum estimate (at some range location) is

$$\hat{S}(k) = \left| \frac{1}{M} \sum_{m=0}^{M-1} V(m) e^{-j \frac{2\pi mk}{M}} \right|^2, \quad k = 0, 1, \dots, M-1 \quad (6)$$

The discrete inverse Fourier transform applied to (6) produces the value of circular autocorrelation function at lag 1 (i.e., T_s) which contains one erroneous term, namely the product of first and last member of the time series (Torres et al., 2007). This term is subtracted so that the autocorrelation at lag one (i.e., T_s) becomes

$$\hat{R}(1) = \sum_{m=0}^{M-1} \hat{S}(k) e^{j \frac{2\pi k}{M}} - \frac{1}{M} V^*(M-1)V(0), \quad (7)$$

and the mean velocity estimate comes out to be (Doviak & Zrnic, 2006. eq 6.19)

$$\hat{v} = -\left(\frac{\lambda}{4\pi T_s}\right) \arg[\hat{R}(1)]. \quad (8)$$

The spectrum width for most VCPs is estimated by combining the lag one autocorrelation

and the signal power $\hat{P}_s = \sum_{m=0}^{M-1} |V(m)|^2 - P_n$, from which the noise power P_n is subtracted, as follows (Doviak & Zrnic 2006, eq 6.27)

$$\hat{\sigma}_v = \frac{\lambda}{2\sqrt{2}\pi T_s} \left| \ln \left(\frac{\hat{P}_s}{|\hat{R}(1)|} \right) \right|^{1/2}. \quad (9)$$

But, if the logarithm term is negative $\hat{\sigma}_v$ is set to zero. In case of phase coding and presence of overlaid echoes equation (9) is used for the weaker signal in the surveillance scan (long PRT). The spectrum width of the strong signal is computed for the Doppler scan using the ratio $\hat{R}(1) / \hat{R}(2)$ as in Doviak & Zrnic (2006, eq. 6.32), because it is not biased by presence of the weak signal.

3.5 Oversampling in azimuth (overlapping radials)

Until recent upgrades all VCPs had spacing of radials at 1° azimuth and reflectivities were averaged and recorded at 1 km range intervals but velocities retained inherent spacing of 250 m (Table 1). Newly added VCPs employ a strategy whereby at the lowest two elevations time series data from overlapping (in azimuth) beams are processed to produce spectral moments. Thus data obtained over one degree azimuth are weighted with the von Hann

window and so are data from the adjacent azimuth centered 0.5° off from the previous. This produces more radials of data (spaced by 0.5° as opposed to 1°) increasing resolution to facilitate recognition of small phenomena such as tornado vortices (Brown et al., 2002, and 2005). The contrast between the routine and enhanced resolution of a tornado vortex signature is evident in the example in Fig. 9. The reflectivity field (top figures in dBZ as indicated by the color bars) displays a “hook echo” associated with low level circulation. The crisp pattern (top right) is the result of the enhanced resolution.

The velocity field (bottom in Fig. 9) displays three circular features (“balls”) in its center: the lighter green and red adjacent to it in azimuth indicate cyclonic circulation (mesocyclone). Its diameter is about four km and it is estimated from the distance between maximum inbound (green) and outbound (red) velocities. The sharp discontinuity in the center (light green ~ -30 m s⁻¹ to > 30 m s⁻¹) is the tornado vortex signature (TVS). The transition between the red “ball” and the green one farther in range marks the zero radial velocity suggesting converging flow (i.e., red and green velocities pushing air toward each other) near ground. Bottom right: same as in the left but the resolution in azimuth is enhanced to 0.5°. The TVS is better defined and so are other small scale features.

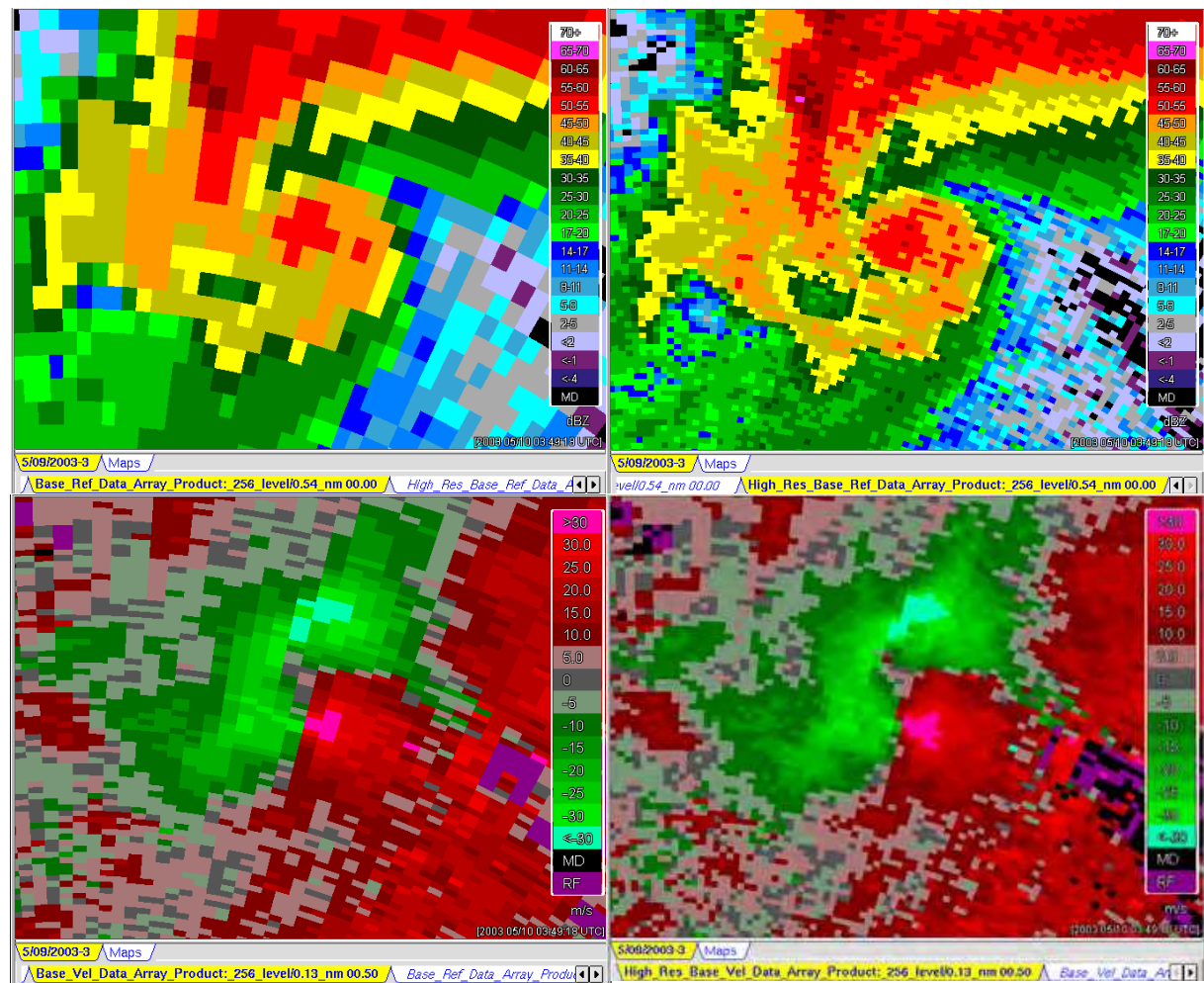


Fig. 9. Top Left: Z, resolution 1 km x 1°. Right: resolution 250 m x 0.5°. Bottom Left: V field, resolution 250 m x 1°. Right: resolution 250 m x 0.5°. X, Y sizes are 25 by 20 km; radar is at x= 4 km and y = -25 km with respect to each image left corner. (Courtesy, S. Torres).

4. Near term enhancements

Currently a significant transformation of the radars is ongoing; it is addition of dual polarization (Zrnic et al., 2008). By mid 2013 all radars on the network should have this capability. Although Doppler capability is not a prerequisite for dual polarization, the coherency of transmit-receive signals within one PRT is for differential phase measurement. Dual polarization offers ample possibilities for application of spectral analysis to polarimetric signals and these are being explored (e.g., to discriminate between insects and birds, Bachman & Zrnic, 2007; to suppress ground clutter, Unal, 2009; or to achieve adaptive clutter and noise suppression, Moisseev & Chandrasekar, 2009).

Three improvements approved for soon inclusion on the network are pending. These are staggered PRT, processing of range oversampled signals, and adaptive recognition and filtering of ground clutter. Brief description follows.

4.1 Staggered PRT

It is planned for mitigating range velocity ambiguities at mid elevation angles with possible use at the lower elevations. The scheme consists of alternating interval between transmitted pulses (Fig. 10) and estimating arguments of two autocorrelations at the two lags, $\arg[R(T_1)]$ and $\arg[R(T_2)]$. The velocities estimated from these arguments have a different unambiguous interval (each inversely proportional to the corresponding separation T_i , $i=1$ or 2) as can be deduced from eq. (8). Therefore the difference of the velocities uniquely tags the proper unambiguous interval for either PRT so that correct dealiasing can be achieved (Torres et al., 2004a) up to larger v_a than possible with only one of these PRTs. For the example in Fig. 10, $v_a = 3v_{a2} = 2v_{a1}$. Consider $T_1=1$ ms $T_2=1.5$ ms which produces $v_a = 50$ m s⁻¹ (unambiguous interval is -50 to 50 m s⁻¹) and unambiguous range of at least 150 km.

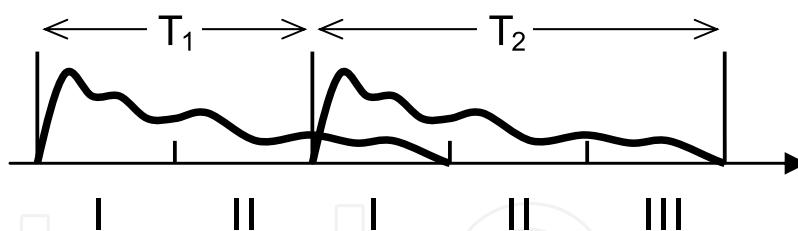


Fig. 10. Staggered PRT. The stagger ratio $T_1/T_2 = 2/3$. The continuous curve depicts the return from precipitation extending up to $cT_2/2$ but not further (from Torres et al., 2009 and adapted from Sachidananda & Zrnic, 2003).

Power estimates in range sections I, II, and III (Fig.10) are computed separately for the short PRT and the long PRT to check if data censoring is needed. Comparison of powers in the two PRT intervals indicates if there is overlay and how severe it is so that appropriate censoring can be applied. In Fig. 11 contrasted are two fields of velocities obtained with two radars (spaced about 20 km apart). The left field comes from the operational WSR-88D in Oklahoma City and was obtained with the “batch mode” and parameters as indicated. On the right is the same storm complex but obtained with staggered PRT on the research WSR-88D radar in Norman OK some 20 km SSW from Oklahoma City. Highlighted in yellow circles are regions where significant aliasing occurs on the operational radar (exemplified by abrupt discontinuities in the field, change from red to green) but are absent in the field from

the research radar. Also, the large pink area of overlaid echoes has almost disappeared in the measurement made utilizing the staggered PRT. The small circle closest to the radar origin indicates overlaid echo contaminating the first trip velocities of the operational radar.

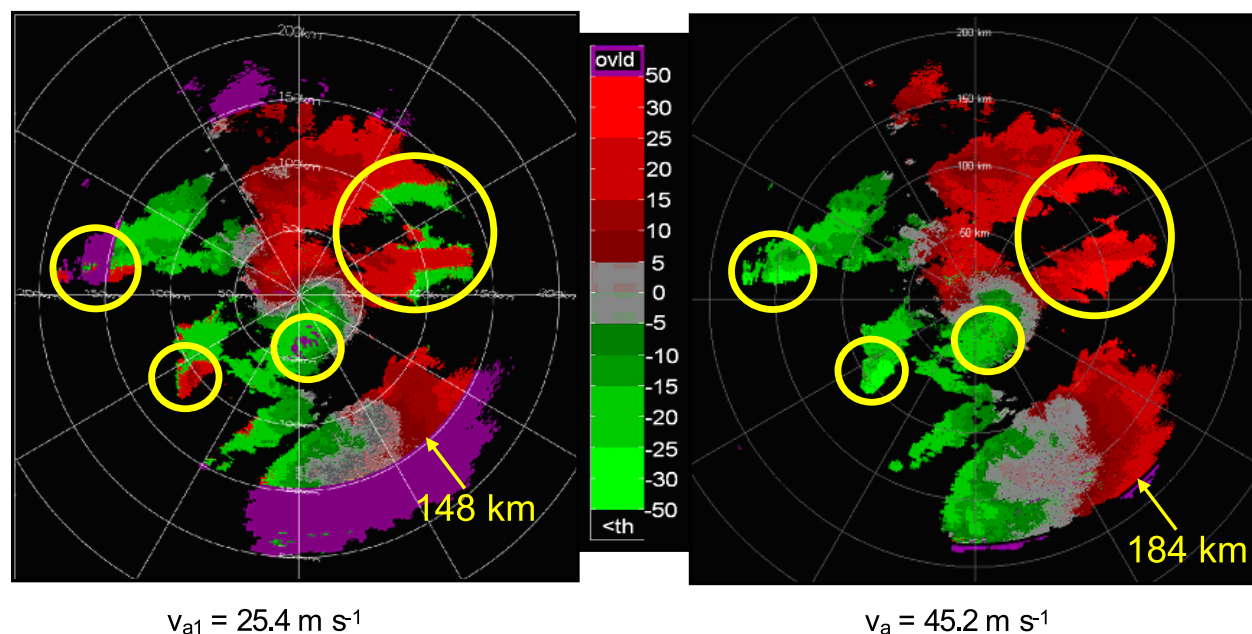


Fig. 11. Velocity fields of a storm system. Left: field obtained with the operational WSR-88D radar in Oklahoma City on April 06, 2003, elevation 2.5 deg, batch mode with unambiguous range of 148 km and velocity of 25.4 m s⁻¹. Pink regions locate censored velocities which can not be reliably recovered due to overlaid first and second trip echoes. Right: same as on the left but obtained with the research WSR-88D (KOUN) utilizing staggered PRT. This radar is about 20 km south from the operational radar. The color bar indicates velocities (m s⁻¹), red away from and green toward the radar. (Figure adapted from Torres et al., 2003).

4.2 Oversampling techniques

Oversampling here indicates spacing of I, Q samples smaller than the pulse duration. Operations on few of these range consecutive “oversamples” can reduce error in estimates and/or data acquisition time (Torres & Zrnic, 2003). Simplest of operations is averaging in range of oversampled spectral moments. Somewhat more involved is the whitening transformation in which the signal vector $\mathbf{v} = [V(m,0), V(m,1), \dots, V(m,l), \dots, V(m,L)]$ consisting of L oversampled correlated complex voltages is transformed into a set of L orthogonal voltages (Torres & Zrnic, 2003). The time index m refers to the usual sample time and l to the oversampled range time. The transformation takes the form $\mathbf{x} = \mathbf{H}^{-1} \mathbf{v}$ with \mathbf{H} related to the normalized correlation matrix \mathbf{C} of \mathbf{v} via $\mathbf{C} = \mathbf{H}^* \mathbf{H}^T$. The correlation matrix can be pre-computed (or measured e.g., Ivic et al., 2003) because it depends solely on the envelope of the transmitted pulse and the baseband equivalent receiver filter shape for a uniform Z . The L transformed samples are independent and averaging of spectral moments obtained from each (in absence of noise) yields smaller error of estimates. Whitening is effective at large SNRs but fails otherwise. To achieve L independent samples the receiver filter bandwidth needs to be increased L times over the matched filter bandwidth and this enhances the noise by the same factor. In addition the whitening transformation also increases the noise hence

the net SNR reduction is proportional to L^2 . Practical L is about 3 to 6, so the decrease is not catastrophic considering that weather SNRs are mostly larger than 20 dB. Another issue concerning whitening is the shape of the range weighting function compared to the matched filter. The two weighting functions have the same range extent but the one from whitening has rectangular shape smearing slightly its range resolution.

Increasing the number of independent samples when it is advantageous and gradually reverting to the matched filter has also been proposed (Torres et al. 2004b) and implemented (Curtis & Torres, 2011) on the National Weather Radar Testbed (NWRT), a phased array radar antenna powered by a WSR-88D transmitter (Zrnic et al., 2007). The processing is called adaptive pseudowhitening. It requires initial estimates of SNR and spectrum width.

Vivid example contrasting adaptive pseudowhitening to standard processing illustrates the much smoother fields obtained with the former (see Fig.12, and caption). The gradient of Doppler velocities (indicated with an arrow) is at the interface of the storms outflow and the environmental flow. This type of discontinuity is the key feature detected by algorithms for locating gust fronts and quantifying wind shear across the boundary; such information is extremely useful for air traffic management and safety at airports.

In contrast to whitening techniques pulse compression does not degrade the SNR (Doviak and Zrnic, 2006) but is not considered due to excessive bandwidth and current hardware constraints. A very simple alternative to speed volume coverage at lowest elevations (where tornadoes are observed) is a VCP with adaptive top elevation angle based on radar measurements (Chrisman et al., 2009). It will soon be added to the VCPs on the network.

4.3 Clutter detection and filtering

A novel way to recognize and filter ground clutter is planned. Its acronym CLEAN-AP stands for clutter environment analysis using adaptive processing (Warde & Torres, 2009). The essence of the technique is spectral analysis (decomposition) of the autocorrelation at lag 1 and use of its phase at and near zero Doppler shift. The conventional estimate

$$\hat{R}_b(1) = \frac{1}{M^2} \sum_0^{M-1} |Z(k)|^2 e^{j2\pi k/M}, \quad (10)$$

where $Z(k)$ is the discrete Fourier transform of the returned signal, is biased (indicated by subscript b) and can be unbiased as in (7). Another way to avoid the bias is by computing two Fourier transform as proposed by (Warde & Torres 2009). One, $Z_0(k)$ is the complex spectrum of $d(m)V(m)$, $d(m)$ =window function, and the other $Z_1(k)$ is the spectrum of $d(m)V(m+1)$ from the sequence shifted in time by one unit (T_s). Then the unbiased estimate is

$$\hat{R}(1) = \sum_{k=0}^{M-1} Z_0^*(k)Z_1(k) / M^2. \quad (11)$$

Individual terms $S_1(k) = Z_0^*(k)Z_1(k)$ constitute the spectral density (over Doppler index k) of the lag 1 autocorrelation function. Thus the autocorrelation spectral density is estimated in CLEAN-AP from the cross spectrum.

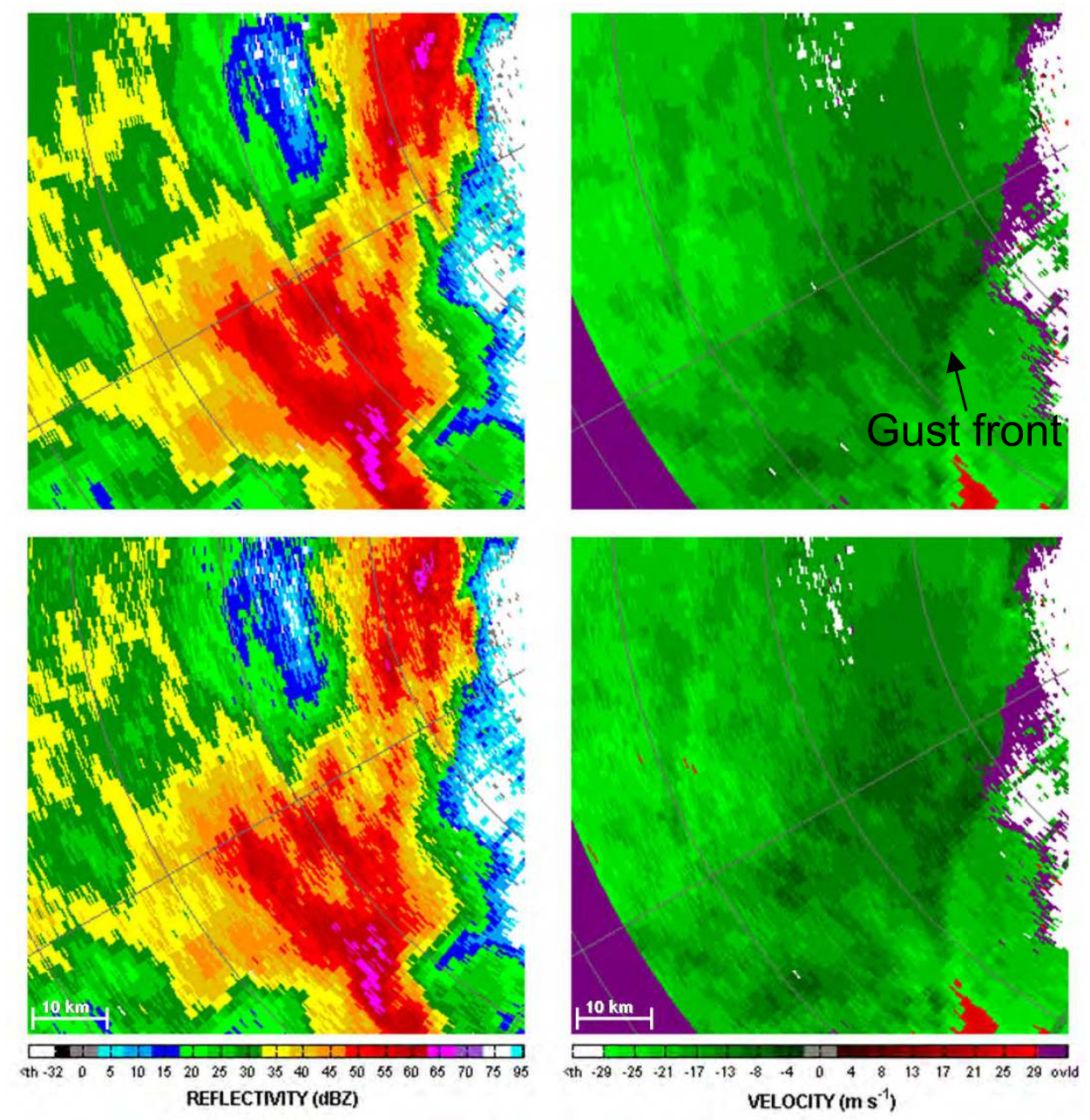


Fig. 12. Fields of reflectivity and velocity from a severe storm obtained on 2 Apr 2010 10:54 UTC, with the phased array radar (NWRT) in Norman, OK. Top two panels resulted for pseudowhitening applied to $L = 4$ samples of time series data; the number of samples M per radial was 12 for Z and 26 for v . Data in the lower panels have been obtained by processing as on the WSR-88D (16 for Z and 64 for v). The curved discontinuity in the velocity field delineates outflow boundary (gust front) generated by this storm. The peak reflectivity values of ~ 65 dBZ are likely caused by hail. (Adapted from Curtis & Torres, 2011).

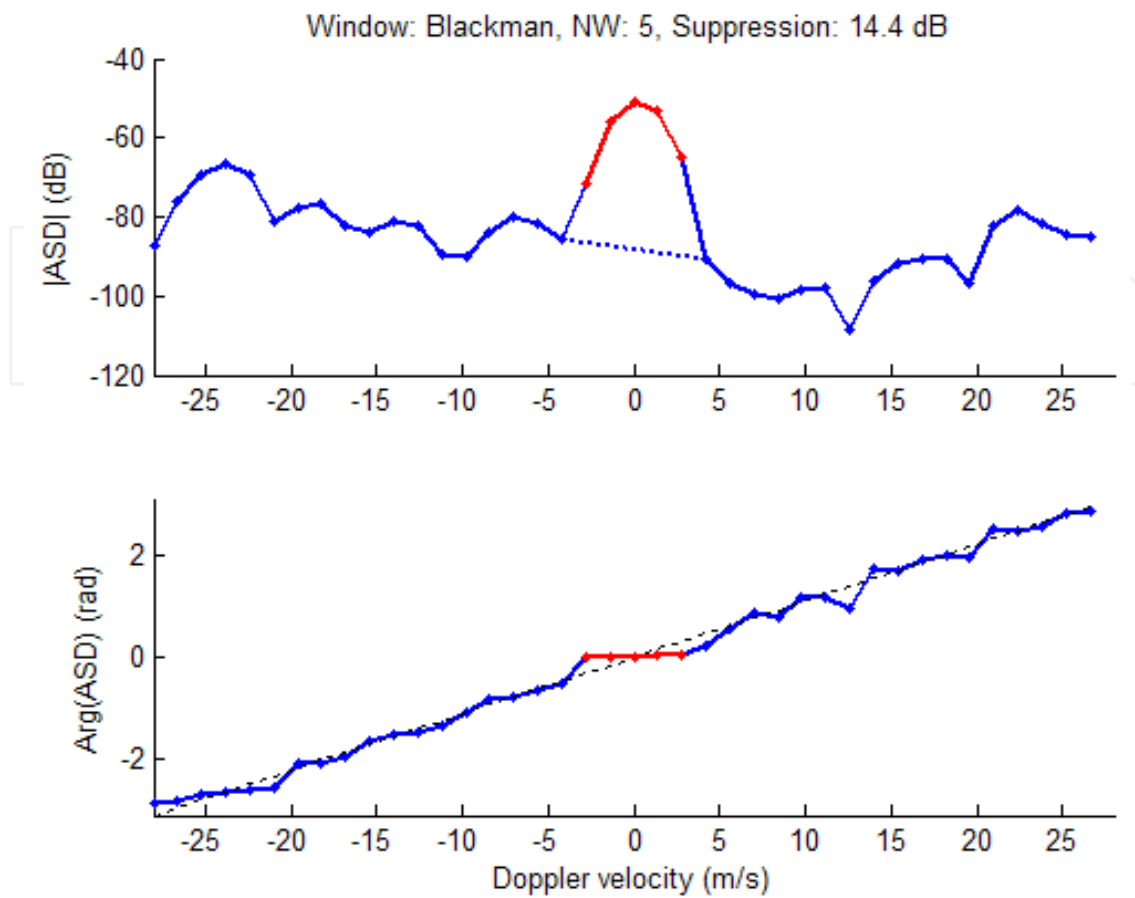


Fig. 13. Autocorrelation spectral density (ASD) of a radar return, top: magnitude and bottom: phase. Clutter is well defined with its peak at zero and flat phase (red). Based on this phase five coefficients are replaced with interpolated values resulting in 14.4 dB of suppression (defined as the ratio of total S+C power to remaining power). Interpolated powers are indicated by the dotted line; dash line represents linear phase; $v_a = 27 \text{ m s}^{-1}$. Data obtained with the phased array radar (NWRT). (Figure courtesy of Sebastian Torres).

The choice of window function $d(m)$ is very important because its sidelobes limit the amount of power that can be filtered. The clutter power is computed from the sum of $V(m)$ to obtain the clutter to noise ratio (CNR). Then the CNR is compared with the peak to first sidelobe level (PS_w) ratio of four windows (w =rectangular, von Hann, Blackman, and Blackman-Nuttall) and the window whose PS_w exceeds the CNR by the smallest amount is chosen. That way the leakage of the clutter signal away from zero will be below the noise level, while the notch width will be smaller than the one for the other windows satisfying the condition $PS_w > \text{CNR}$.

Data windows spread the phase of clutter's $S_1(k)$ either side of zero ($k=0$) Doppler (Fig. 13). Recognition of the flat phase identifies clutter's presence. Doppler index at which the phase begins to depart from zero (according to a set of criteria) defines the clutter filter width. In the mean the autocorrelation spectral density of noise has linear phase as seen in Fig.13 but semi coherent signals have flattened phases in the vicinity of their mean Doppler shifts. Panels in Fig. 14 demonstrate qualitative performance of this clutter mitigation technique and the caption highlights results.

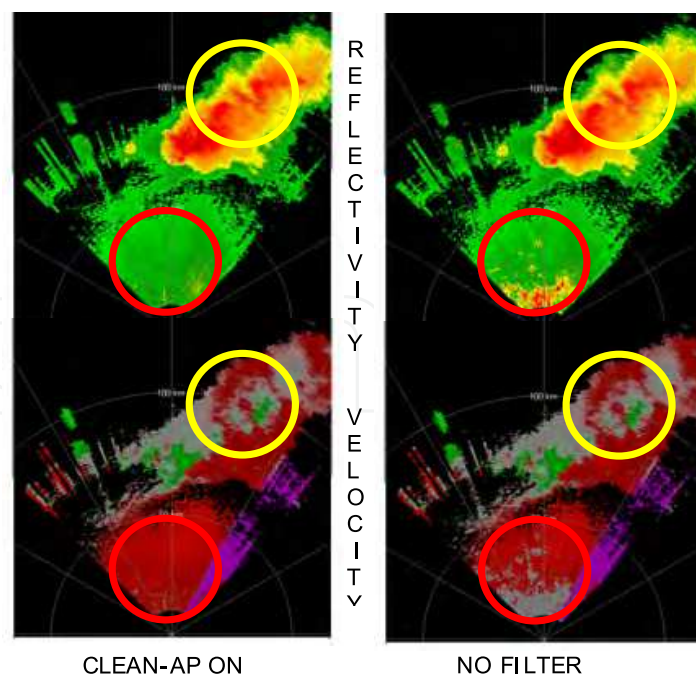


Fig. 14. Fields of reflectivities (top) and velocities (bottom) with no filter (right) and after application of the CLEAN-AP. Close to the radar the strong reflectivities in the top right panel encircled in red (red indicates > 50 dBZ) are caused by ground clutter which also biases the velocities toward zero (lower right panel). CLEAN-AP eliminates most of the clutter in both fields (left panels). To the NE within the yellow circle there are areas of near zero velocities (lower panels gray areas are velocities within ± 5 m s $^{-1}$). These appear unaffected by the filter. The data were collected with the agile beam phased array radar (NWRT) in Norman, OK. (Figure adapted from Warde & Torres, 2009).

4.4 Hybrid spectrum width estimator

The spectrum width estimator (9) is deficient at narrow widths where significant bias occurs. This shortcoming will be overcome with the Hybrid estimator which chooses an appropriate equation depending on a rough initial estimate of σ_v (Meymaris et al., 2009). Initial estimate of the spectrum width is made using three estimators (9), $\hat{R}(1)/\hat{R}(2)$ as in (Doviak & Zrnic, 2006 eq. 6.32) and an estimator based on $\hat{R}(1)$, $\hat{R}(2)$, and $\hat{R}(3)$. Criteria applied to the results produce three categories of widths, large, medium, and small. Then (9) is used as estimate for the large category, $\hat{R}(1)/\hat{R}(2)$ for the medium and $\hat{R}(1)/\hat{R}(3)$ for the small.

5. Observations of phenomena

Mesocyclone refers to a rotational part of storm with the diameter of maximum wind typically between 3 and 10 km. It is depicted with a couplet of Doppler velocity features (see Fig. 9). Storms having mesocyclones can produce devastating tornadoes (Fig. 9 exhibits a tornado vortex signature associated with the mesocyclone), strong winds, and hail. Thus, much effort has been devoted to detecting and quantifying these phenomena (No. 2 issue of Weather and Forecasting, 1998). One of the motivating reasons for installing Doppler radars

in the USA was the potential to detect mesocyclones and tornadoes. The investment in this technology paid off as demonstrated by the graph in Fig. 15. Trend of improvement is seen on all three performance indicators with the steepest rise in the years the Doppler radar network (NEXRAD) was being installed. This is logical: as the new tool was spreading across the country more forecasters were beginning to use it. Improvement continues few years past the completion of the network likely because it took time to train all forecasters and gain experience with the Doppler radar. The data indicates a plateau from about 2002 until present suggesting maturity of the technology with little room left for significant advancements. Further progress might come from combining radar data with short term numerical weather prediction models and/or introduction of rapidly scanning agile beam phase array radars (Zrnice et al., 2007 and Weber et al., 2007).

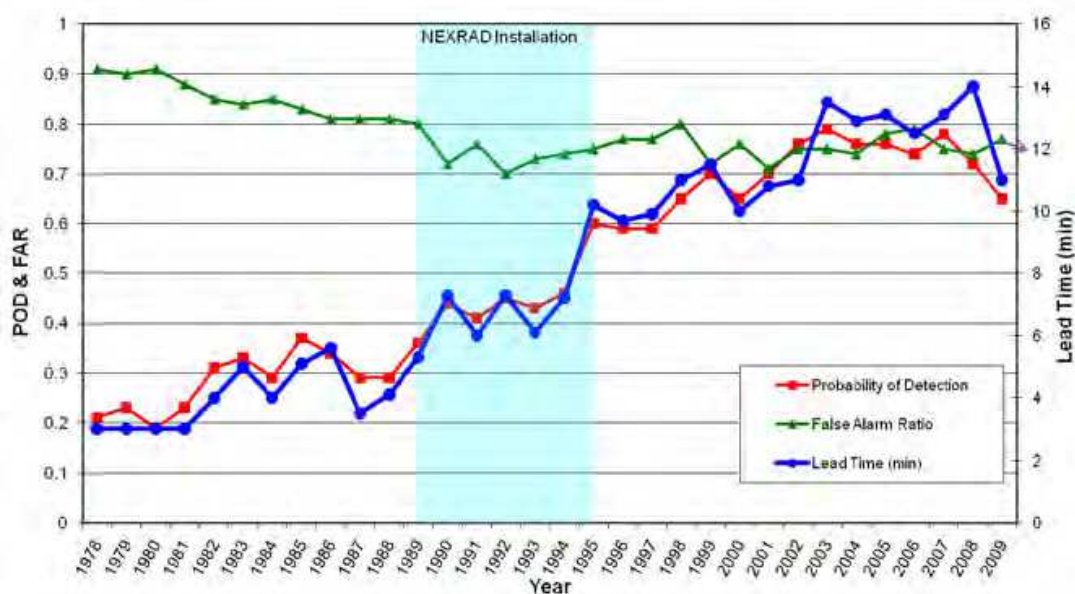


Fig. 15. Probability of detection, false alarms and lead time in tornado warnings issued by the National Weather Service as function of year. (Figure courtesy Don Burgess).

Doppler velocities are potent indicators of diverging (converging) flows such as observed in strong outflows from collapsing storms. These “microbursts” have been implicated in several aircraft accidents motivating deployment of terminal Doppler weather radars (TDWR) at forty seven airports in the USA (Mahapatra, 1999, sec 7.4). Vertical profiles of reflectivity and Doppler velocity in Fig. 16 indicate a pulsing microburst; the intense reflectivity core (red below 5 kft) near ground is the first precipitation shaft and the elongated portion above is the following shaft. On the velocity display the yellow arrows indicate direction of motion. Clear divergence near ground and at the top of the storm (in the anvil) is visible and so is the convergence over the deep mid storm layer (5 to 14 kft). The horizontal change in wind speed near ground of ~ 20 kts at this stage is not strong to pose treat to aviation (35 kts is considered significant for light aircraft).

An atmospheric undular bore (Fig. 17) was observed with the WSR-88D near Oklahoma City. This phenomena is a propagating step disturbance in air properties (temperature, pressure, velocity) followed by oscillation. Spaced by about 10 km the waves propagate in a surface-based stable layer. The layer came from storm outflow and the bore might have been

generated by subsequent storm. From the vertical cross section of the velocities it is evident that the positive velocity perturbation (toward the radar) ends at about 4000 ft, above which the ambient flow (green color) resumes. The velocities measured by the radar can quantify the structure of the perturbation, tell the thickness and wavelength. Propagation speed can be estimated by tracking the wave position in space and time.

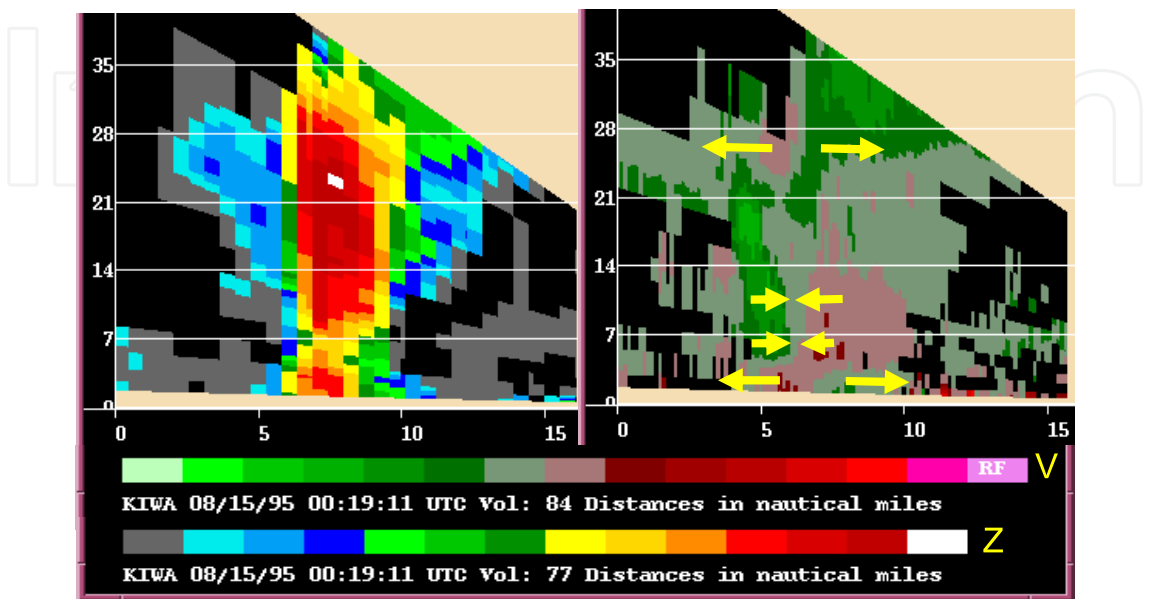


Fig. 16. Vertical cross sections of reflectivity field (left) and Doppler velocity field through a microburst reconstructed from conical scans (up to 19.5° elevation) of the WSR-88D radar in Phoenix Az on Aug 15, 1995. Height is in kft and distances are in nautical miles. The radar is located to the right of each cross section (at about 26 nautical miles). The top color bar depicts velocity categories in non linear increments with red away from the radar: light red = 0-5 kts, dark red 5 to 10, next 10-20; green indicates toward the radar in categories symmetric to red. The bottom bar refers to reflectivities starting at 0 dBZ in steps of 5 dBZ (white category indicates values larger than 65 dBZ).

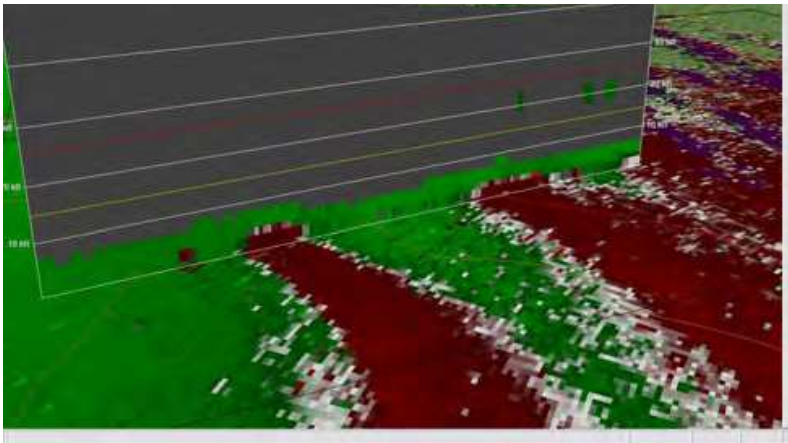


Fig. 17. Doppler velocities at 0.5° elevation and superposed vertical cross sections of the velocities obtained with Oklahoma City radar on Aug 10, 2011. Red color indicates motion away and green toward the radar located ESE of the bottom right corner. Height lines are in kft above ground level.

Doppler radar is valued for measuring winds in hurricanes and detecting tornadoes that can be imbedded in the bands. Combined with polarimetric capability, its utility greatly increases because of improved quantitative measurement of rainfall. Observation of hurricane Irene which swept the US East coast at the end of August 2011 is the case in point. Rotation speed of over 110 km h^{-1} is apparent in Fig. 18 where the color categories are too coarse to estimate the maximum values. The cyan color captures well Irene's rotational winds because they are aligned with radials. Color categories are coarse precluding precise estimation of velocities but recorded values are quantized to 0.5 m s^{-1} . Although the unambiguous velocity is $\sim 28 \text{ m s}^{-1}$ values more negative than -30 m s^{-1} are displayed. These and other outside the unambiguous interval have been correctly dealiased by imposing spatial continuity to the field.

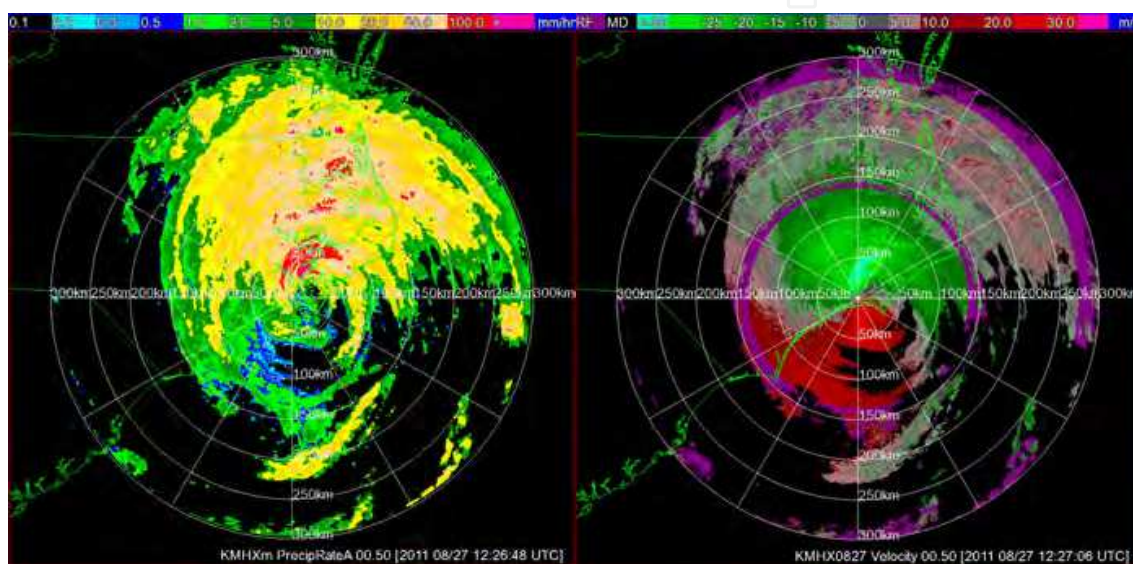


Fig. 18. Left: Rain rate in Hurricane Irene, obtained with a polarimetric algorithm using differential phase and reflectivity factor (surveillance scan with unambiguous range of $\sim 465 \text{ km}$). Right: Velocity field obtained with the SZ(2) phase code (Doppler scan with unambiguous range of $\sim 135 \text{ km}$ and velocity $\sim 28 \text{ m s}^{-1}$). Elevation is 0.5° , time 12:26 UTC, on Aug 27, 2011. The range circles are spaced 50 km apart. Color categories for rain rate are in mm h^{-1} and for velocity in m s^{-1} . (Figure courtesy of Pengfei Zhang).

The rain rate field depicts Irene's bands some containing values larger than 100 mm h^{-1} . These are instantaneous measurements and over time accumulations caused significant flooding which brought 43 deaths and ~ 20 billion \$ damage to the NE coast of the USA. The obviously large spatial extent of Irene amply justifies use of surveillance scan for maximum storm coverage and Doppler scan for wind hazard detection.

Atmospheric biota is routinely observed with the WSR-88D network (Rinehart, 2010). Examples are insects, birds, and bats. Many insects are passive wind tracers providing a way to estimate winds in the planetary boundary layer (extending up to 2 km above ground).

Biota can be tracked for ecological or other purposes. The radar can also provide location of bird migrating paths, roosts, and other congregating places; this could be important for aircraft safety. The three donut shaped features in Fig. 19 represent Doppler speeds of birds

leaving roost early in the morning. The critters are diverging away from the roost in search of food. Close to the radar the continuous field of velocities is principally from reflections off insects filling a good part of the boundary layer (this is deduced from polarimetric signatures, but not shown here).



Fig. 19. Field of velocities obtained from the radar at Moorhead City, NC, on July 27, 2011 at 5:08 in the morning. The color bar indicates categories in kts; red away from the radar and green is toward. Elevation is 0.5°.

6. Epilogue

The WSR-88D network has been indispensable for issuing warnings of precipitation and wind related hazards in the USA. And its real time display of storm locations has become one of most popular and common applications on cellular phones. Its role in quantitative precipitation estimation is matching that of rain gages. So, what is beyond these achievements for the WSR-88D? Dual polarization upgrade combined with Doppler capability is the panacea a radar with the dish antenna on a rotating pedestal can achieve. Promising possibilities are: polarimetric confirmation of tornado touchdown at places where Doppler velocities indicate rotation; improvement of ground clutter filtering; polarimetric spectral analysis for extracting/separating features within radar resolution volume; significant improvement in data interpretation; inclusion of wind and precipitation type/amount in numerical prediction models; and other. Clearly the evolutionary trend continues and will do so at a decelerating pace until a plateau is reached. Complementary shorter wavelength (3 cm and 5 cm) surveillance radars are being considered for closing gaps or providing extra coverage at opportune places. (The TDWRs 5 cm wavelength radar data has been supplied to the NWS for several years). Explored are networks of tightly coordinated 3 cm wavelength radars for surveillance close to the ground.

One emerging technology is rapid scan agile beam phased array radar. This might be the ultimate radar providing it exceeds all the capabilities on the current network at faster scan rates. If in addition it proves to fulfill security and aviation needs (tracking of airplanes, missiles) it could revolutionize the current radar paradigm.

7. Acknowledgment

The author is grateful to Rich Ice, Darcy Saxion, Alan Free, and Dave Zittel for advice and valuable information about the WSR-88D. Sebastian Torres provided several figures and comments concerning technical aspects and designed signal processing for the MPAR. Dave Warde contributed figures and details about ground clutter and some VCPs. Collaboration with Dick Doviak is reflected in the requirements section. Allen Zahrai was in charge of engineering developments on MPAR and KOUN; Doug Forsyth lead the MPAR team in outstanding support and development of that platform.

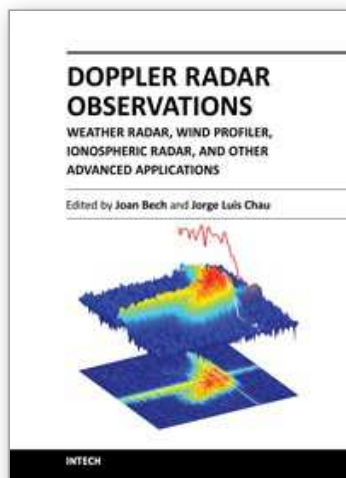
8. References

- Bachmann, S., & D. Zrníc (2007). Spectral Density of Polarimetric Variables Separating Biological Scatterers in the VAD Display. *J. Atmos. Oceanic Technol.*, Vol. 24, pp.1186-1198.
- Bringi, V. N., & V. Chandrasekar (2001). *Polarimetric Doppler Weather Radar*. Cambridge University Press, Cambridge, UK.
- Brown, R. A., V. T. Wood, & D. Sirmans (2002). Improved tornado detection using simulated and actual WSR-88D data with enhanced resolution. *J. Atmos. Oceanic Technol.*, Vol. 19, pp. 1759-1771.
- Brown, R. A., B. A. Flickinger, E. Forren, D. M. Schultz, D. Sirmans, P. L. Spencer, V. T. Wood, & C. L. Ziegler (2005). Improved detection of severe storms using experimental fine-resolution WSR-88D measurements. *Weather and Forecasting*, Vol. 20, 3-14.
- Burgess, D. W., V. T. Wood, & R. A. Brown (1982). Mesocyclone evolution statistics, *Severe Storm Conf. Proc.*, pp. 422-424, AMS, Boston, MA, USA.
- Chrisman, J.N. (2009). Automated volume scan evaluation and termination (AVSET). *34th Conference on Radar Meteorology*, AMS, Williamsburg, VA, USA.
- Crum, T.D., & R.L. Alberty (1993). The WSR-88D & the WSR-88D operational support facility." *B. American Meteorological Society*, Vol. 74, pp. 1669-1687.
- Crum, T.D., R.L. Alberty, & D.W. Burgess (1993). Recording, archiving, and using WSR-88D data." *B. American Meteorological Society*, Vol. 74, pp. 645-653.
- Curtis, D.C., & S. M. Torres (2011). Adaptive range oversampling to achieve faster scanning and the national weather radar testbed phased array radar. *J. Atmos. Oceanic Technol.*, in press.
- Doviak, R.J., & D. S. Zrníc (2006). *Doppler radar and weather observations*. Second edition, reprinted by Dover, Mineola, NY, USA.
- Free, A.D., & N.K. Patel (2007). Clutter censoring theory and application for the WSR-88D. *32nd Conference on Radar Meteorology*, AMS, Albuquerque, NM, USA.
- Heiss, W.H, D.L McGrew, & D. Sirmans (1990). Next generation weather radar (WSR- 88D). *Microwave J.*, Vol. 33, pp. 79-98.

- Hubbert, J.C., M. Dixon, & S.M. Ellis (2009). Weather radar ground clutter. Part II) Real- time identification and filtering. *Jour. Atmosph. Oceanic. Tech.* Vol. 26, pp. 1181-1197.
- Ice, L.R., & D.S. Saxion (2011). Enhancing the foundational data from the WSR-88D) Part II, the future, *35th Conference on Radar Meteorology*, AMS, Pittsburgh, PA, USA.
- Ivic, R.I., D.S. Zrnic, & S. M. Torres (2003). Whitening in range to improve weather radar spectral moment estimates. Part II) Experimental evaluation. *J. Atmos. Oceanic Technol.*, Vol. 20, pp. 1449-1459.
- Mahapatra, P. (1999). *Aviation weather surveillance systems*. Published by IEE and AIAA, printed by Short Run Press, Ltd, Exeter, UK.
- Meischner, P. (2004). *Weather radar, principles and advanced applications*. Springer-Verlag, Berlin, Germany.
- Meymaris, G., J.K. Williams, & J.C. Hubbert (2009). Performance of a proposed hybrid spectrum width estimator for the NEXRAD ORDA. *25th Int. Conf. on IIPS*. AMS, Phoenix, AZ, USA.
- McLaughlin, D., & Coauthors (2009). Short-wavelength technology and the potential for distributed networks of small radar systems. *Bull. Amer. Meteor. Soc.*, Vol. 90, pp. 1797-1817.
- Moisseev, D.N., & V. Chandrasekar (2009). Polarimetric spectral filter for adaptive clutter and noise suppression. *J. Atmos. Oceanic Technol.*, Vol. 26, 215-228.
- Rinehart, R.E. (2010). *Radar for meteorologists*. Fifth edition. Rinehart Publications, Nevada, MO, USA.
- Sachidananda, M., & D.S. Zrnic (2003). Unambiguous Range Extension by Overlay Resolution in Staggered PRT Technique. *J. Atmos. Oceanic Technol.*, Vol. 20, pp. 673-684.
- Sachidananda, M., & D.S. Zrnic (1999). Systematic phase codes for resolving range overlaid signals in a Doppler weather radar. *J. Atmos. Oceanic Technol.*, Vol. 16, pp. 1351-1363.
- Saxion, D. S., & R. L. Ice (2011). Enhancing the foundational data from the WSR- 88D) Part I, a history of success. *35th Conference on Radar Meteorology*, AMS, Pittsburgh, PA.
- Serafin, R.J. & J.W. Wilson (2000). Operational weather radar in the United States Progress and opportunity. *Bull. Amer. Meteor. Soc.*, Vol. 81, pp. 501-518.
- Siggia, A.D., & R. E. Passarelli, Jr. (2004). Gaussian model adaptive processing (GMAP) for improved ground clutter cancellation and moment calculation. *Proceedings of ERAD (2004)*, pp. 67-73. Visby, Island of Gotland, Sweden.
- Torres, M.S., C.D. Curtis, D.S. Zrnic, & M. Jain (2007). Analysis of new Nexrad spectrum width estimator. *33rd Inter. Conf. on Radar Meteorology*, AMS, Cairns, Australia.
- Torres, M.S., Y.F. Dubel, & D.S. Zrnic (2004a). Design, implementation, and demonstration of a staggered PRT algorithm for the WSR-88D. *J. Atmos. Oceanic Technol.*, 21, 1389-1399.
- Torres, M.S., C.D. Curtis, & J.R. Cruz (2004b). Pseudowhitening of weather radar signals to improve spectral moment and polarimetric variable estimates at low signal-to-noise ratios. *IEEE Trans. Geosc. Remote Sens.* Vol. 42, pp. 941-949.
- Torres S., Sachidananda, M, & D. Zrnic (2004c). Signal Design and Processing Techniques for WSR-88D Ambiguity Resolution) Phase coding and staggered PRT, implementation, data collection, and processing. NOAA/NSSL Report, Part 8, available from http://publications.nssl.noaa.gov/wsr88d_reports/.

- Torres S., D. Zrnic, & Y. Dubel (2003). Signal Design and Processing Techniques for WSR-88D Ambiguity Resolution) Phase coding and staggered PRT, implementation, data collection, and processing. NOAA/NSSL Report, Part 7, available from http://publications.nssl.noaa.gov/wsr88d_reports/.
- Torres, S.M., & D.S. Zrnic (2003). Whitening in range to improve weather radar spectral moment estimates. Part I) Formulation and simulation. *J. Atmos. Oceanic Technol.*, Vol. 20, pp. 1443-1448.
- Unal, C. (2009). Spectral polarimetric radar clutter suppression to enhance atmospheric echoes. *J. Atmos. Oceanic Technol.*, Vol. 26, pp. 1781-1797.
- Warde, A. D., & S. M. Torres (2009). Automatic detection and removal of ground clutter contamination on weather radars. *34th Conference on Radar Meteorology*, AMS, Williamsburg, VA, USA.
- Weber, M., J.Y.N. Cho, J.S. Flavin, J. M. Herd, W. Benner, & G. Torok (2007). The next generation multi-mission U.S. surveillance radar network. *Bull. Amer. Meteorol. Soc.*, Vol. 88, pp. 1739-1751.
- Wood, V.T, R. A. Brown, & D. Sirmans (2001). Technique for improving detection of WSR-88D mesocyclone signatures by increasing angular sampling. *Weather and Forecasting*. Vol. 16, pp. 177-184.
- Zittel, W.D. , D. Saxion, R. Rhoton, & D.C. Crauder (2008). Combined WSR-88D technique to reduce range aliasing using phase coding and multiple Doppler scans. *24th IIPS Conference*, AMS. New Orleans.
- Zrnic, D. S., J. F. Kimpel, D. F. Forsyth, A. Shapiro, G. Crain, R. Ferek, J. Heimmer, W. Benner, T. J. McNellis, & R. J. Vogt (2007). Agile beam phased array radar for weather observations. *Bull. Amer. Meteorol. Soc.*, Vol. 88, pp. 1753-1766.
- Zrnic, D., S. V. M. Melnikov, & I. Ivic, 2008: Processing to obtain polarimetric variables on the ORDA (final version) NOAA/NSSL Report available from http://publications.nssl.noaa.gov/wsr88d_reports/.

IntechOpen



Doppler Radar Observations - Weather Radar, Wind Profiler, Ionospheric Radar, and Other Advanced Applications

Edited by Dr. Joan Bech

ISBN 978-953-51-0496-4

Hard cover, 470 pages

Publisher InTech

Published online 05, April, 2012

Published in print edition April, 2012

Doppler radar systems have been instrumental to improve our understanding and monitoring capabilities of phenomena taking place in the low, middle, and upper atmosphere. Weather radars, wind profilers, and incoherent and coherent scatter radars implementing Doppler techniques are now used routinely both in research and operational applications by scientists and practitioners. This book brings together a collection of eighteen essays by international leading authors devoted to different applications of ground based Doppler radars. Topics covered include, among others, severe weather surveillance, precipitation estimation and nowcasting, wind and turbulence retrievals, ionospheric radar and volcanological applications of Doppler radar. The book is ideally suited for graduate students looking for an introduction to the field or professionals intending to refresh or update their knowledge on Doppler radar applications.

How to reference

In order to correctly reference this scholarly work, feel free to copy and paste the following:

Dusan S. Zrníc (2012). Doppler Radar for USA Weather Surveillance, Doppler Radar Observations - Weather Radar, Wind Profiler, Ionospheric Radar, and Other Advanced Applications, Dr. Joan Bech (Ed.), ISBN: 978-953-51-0496-4, InTech, Available from: <http://www.intechopen.com/books/doppler-radar-observations-weather-radar-wind-profiler-ionospheric-radar-and-other-advanced-applications/doppler-radar-for-usa-weather-surveillance>

INTECH
open science | open minds

InTech Europe

University Campus STeP Ri
Slavka Krautzeka 83/A
51000 Rijeka, Croatia
Phone: +385 (51) 770 447
Fax: +385 (51) 686 166
www.intechopen.com

InTech China

Unit 405, Office Block, Hotel Equatorial Shanghai
No.65, Yan An Road (West), Shanghai, 200040, China
中国上海市延安西路65号上海国际贵都大饭店办公楼405单元
Phone: +86-21-62489820
Fax: +86-21-62489821

© 2012 The Author(s). Licensee IntechOpen. This is an open access article distributed under the terms of the [Creative Commons Attribution 3.0 License](https://creativecommons.org/licenses/by/3.0/), which permits unrestricted use, distribution, and reproduction in any medium, provided the original work is properly cited.

IntechOpen

IntechOpen